Universiteit Utrecht

VIRGO

Faculteit Bètawetenschappen

A population of galaxy-lensed gravitational waves

Bachelor Thesis

A. Renske A. C. Wierda

Natuur- en Sterrenkunde

Supervisors:

dr. Otto Akseli Hannuksela
Dutch National Institute for Subatomic Physics

prof. dr. Chris van den Broeck
Institute for Gravitational and Subatomic Physics Utrecht

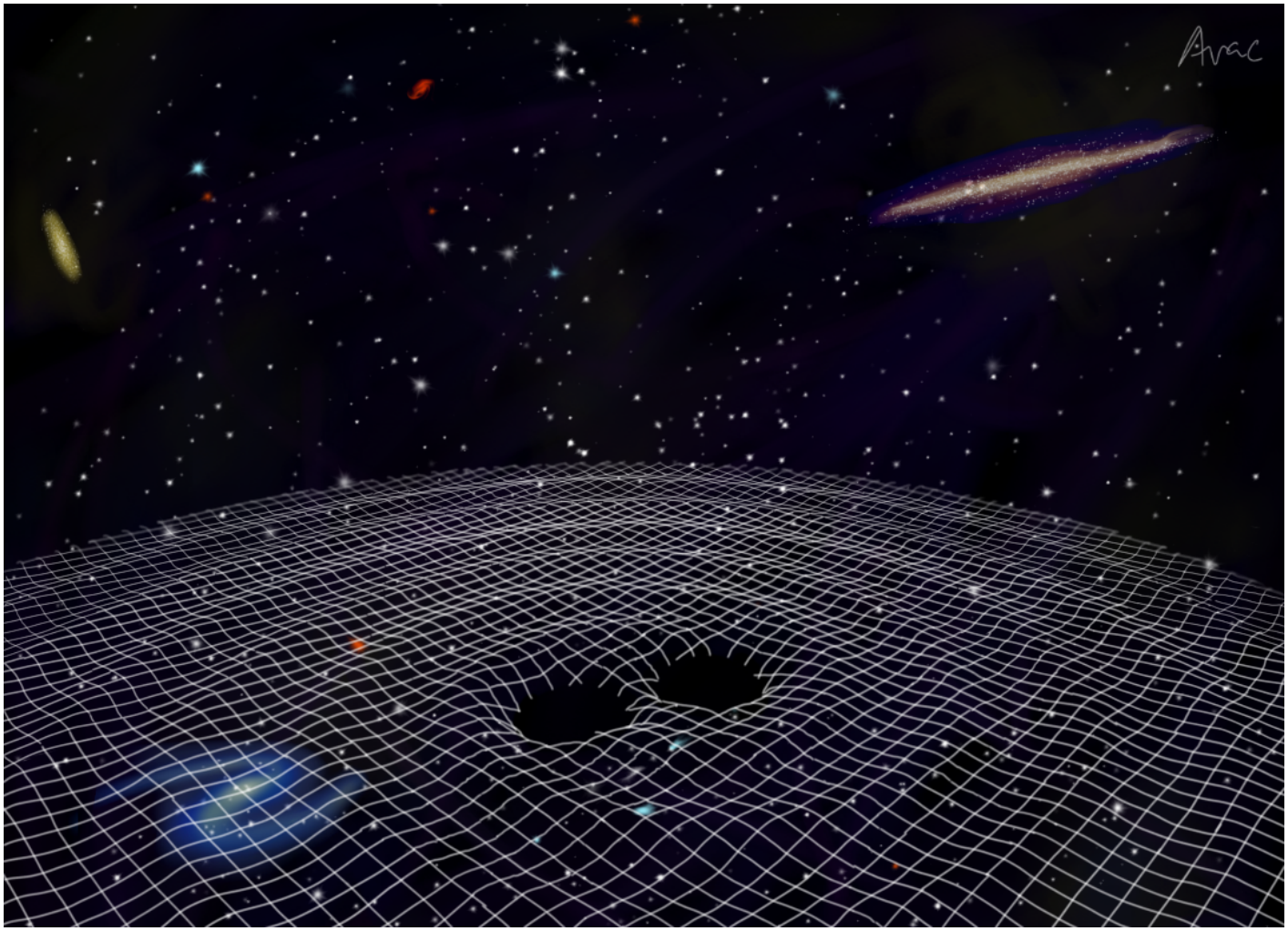

June 16, 2021

Abstract

The coalescence of binary black holes produces gravitational waves, which subsequently can be gravitationally lensed (like light) when passing by massive astrophysical objects, such as galaxies. We observe strong lensing as the occurrence of repeated events (images) with different amplitudes, arriving at different times at our detectors due to travelling along different trajectories.

We build a population of strongly lensed gravitational waves, based on analyses of binary black hole detections and on electromagnetic observations of strong lensing. We investigate the predicted rate of galaxy-lensed event detections for the ground-based LIGO-Livingston, LIGO-Hanford, Virgo and KAGRA gravitational wave detectors, and we forecast $\sim 1-2$ lensed events per year at their design sensitivities. We also show the event rates for the future LIGO detector upgrades A+ and Voyager, and comment on possible improvements by including so-called sub-threshold triggers – gravitational waves buried in noise.

We find most lensed binaries at redshifts $z \sim 1-4$, beyond the regular detector horizon. We report the predicted distributions for lensing parameters, such as the time delay between images. We discuss the impact of lensing statistics on lensed event searches, which rely on comparing pairs of event triggers. However, two unlensed events can have a similar signature within detector accuracy, producing a false alarm. We find that including lensing statistics can improve the significance of a truly lensed event by a factor ~ 30. We argue that the inclusion of lensing statistics is vital for the lensed event searches, as otherwise the occurrence of a false alarm becomes inevitable for long observing runs. We hope that this work will further the case for lensed event searches, and we stress the importance of incorporating lensing statistics into these searches.

Cover image: Artist rendition of the gravitational waves emitted by two inspiraling black holes. Personal work.

Contents

1 Introduction

In 1915, Albert Einstein published his now-famous theory of General Relativity (GR) [1], and revolutionised our view on gravity. Where Newton considered instantaneous forces represented as vectors[1], Einstein saw the 'gravitational force' as merely a result of the curvature of space *and* time together, caused by the presence of mass. It is a dynamical harmony, where mass tells space-time how to curve, and space-time tells mass how to move. The first observational confirmation of the theory came from *gravitational lensing*, where light follows curved paths in spacetime around heavy objects. It was first measured during the total solar eclipse of 1919 by Arthur Eddington, Frank Watson Dyson and their collaborators, who took photographs of stars near the Sun from several locations on Earth [2]. In 1979, the Twin Quasar was discovered, and it became the first identified gravitationally strongly lensed object [3]. These days, gravitational lensing of light is an active field of research. The upcoming Euclid telescope will survey a third of the sky, look back up to 10 Gyr in time, and is projected to measure gravitational lensing effects on 1 billion astronomical sources. These measurements, and other such lensing measurements, can in turn be used for the discovery of exoplanets, probing the expansion history of the Universe and mapping its dark matter contents [4–6].

Central to GR are the Einstein Field Equations (EFE), which are generally non-linear and extremely difficult to solve analytically. In 1916, Karl Schwarzschild found the solutions describing a *black hole* [7], an exotic object with a singularity at its centre and an event horizon from within which nothing can escape, not even light. These bodies were long considered to be mathematical constructs, but in 1971 the X-ray source Cygnus X-1 was found through indirect evidence to be a binary system of a supergiant star and a high mass compact object [8, 9], the first observed black hole. Nowadays, many indirect observations of black holes have been made, and the first direct photo of a supermassive one was published on April 10th 2019 by the Event Horizon Telescope Collaboration [10].

Another exciting prediction from GR is the existence of *gravitational waves* (GWs) [11], which can be produced by large variations in the local mass-density. If the Sun were to disappear this instant, gravitational waves would spread out across the solar system like ripples in a pond, and hit the Earth roughly eight minutes later. Luckily for us, the Sun will not vanish. However, this means we need other sources to measure gravitational waves from. The first indirect observation was from the Hulse-Taylor binary, which has an ever so slightly decreasing orbital period, inline with the emission of gravitational waves [12, 13]. The first direct observation was made on the 14th of September 2015 by the LIGO Scientific Collaboration [14]. The event was labelled GW150914, and consisted of two black holes spiralling towards each other, before finally merging to leave behind a single, heavier black hole. Currently, there are four operational gravitational wave detectors capable of detecting gravitational waves: LIGO-Livingston and Hanford in the United States, Virgo in Italy and KAGRA in Japan. In the Gravitational Wave Transient Catalog 2 (GWTC-2) [15], a total of 50 candidate events are reported. Many more can be expected in the future, with detector upgrades and new detectors coming online.

This turns our attention to an interesting possibility in GR. Gravitational waves travel along the same paths as light, so if they pass by a heavy astrophysical object, they should be lensed in a similar manner to light [16–21]. *Lensed gravitational waves* can become unique probes of GR and cosmology in general, as the detected effects of gravitational-wave lensing are distinctly different from the lensing of light [22]. If observed, lensed gravitational waves would enable us to determine the precise sky localisation of the source of the gravitational wave [23], perform Hubble constant measurements [23–27] and even put alternate theories to GR to the test [28–32]. While lensed gravitational waves have not been detected yet, forecasts indicate that a lensed event detection will become probable in the near future [33–37]. These estimates are mostly based on simplified astrophysical distributions. Here, we will investigate the observed rate of lensed events with a more complex model, allowing for more diverse lensing configurations. We will also comment on the effect of the lensed event searches themselves.

[1] Incidentally, Newton knew his instantaneous action at a distance was most likely wrong. In 1692, he wrote to Richard Bentley: *"That one body may act upon another at a distance through a vacuum without the mediation of anything else, by and through which their action and force may be conveyed from one another, is to me so great an absurdity that, I believe, no man who has in philosophic matters a competent faculty of thinking could ever fall into it."*

In recent years, methodologies have been developed to detect lensed events [38–44], and those have been tested on the currently available datasets as well [45–48]. Strongly lensed gravitational waves appear as multiple triggers with similar signatures in our detectors, so pairs of detection triggers need to be compared during a lensing search. However, there is a chance of two unrelated unlensed events sharing the same signature, which would be a *false alarm*. The number of pairs grows quadratically with the number of detections, making the occurrence of a false alarm increasingly inevitable. We will study the predicted lensing properties of the lensed events, and investigate their capacity to constrain the false alarm probability.

In this work, we will focus on lensing of binary black hole (BBH) mergers, since these are the heaviest astrophysical objects accessible and can thus be detected out to large distances, which is where lensing takes place. We will improve on previous lensing forecasts (Sec. 5.1), with an observationally constrained BBH population from GWTC-2 (Sec. 4.1), and galaxies from the Sloan Digital Sky Survey (SDSS) catalogue (Sec. 4.2). We will also show how predictions from lensing statistics can help improve the searches for lensed gravitational waves (Secs. 5.2 & 5.3), and will finally comment on the science prospects of lensed detections in juxtaposition with our data (Sec. 5.4). Besides this thesis, a brief article featuring our results has also been submitted to ArXiv [49], and the Astrophysical Journal.

2 Gravitational waves

Before we dive into the core of this work, we will start with presenting all the theoretical background necessary for understanding it, and relate the theory to observations. Central to this section is a single set of equations, the *Einstein Field Equation* (EFE):

$$G_{\mu\nu} = \frac{8\pi G}{c^4} T_{\mu\nu} \,. \tag{2.1}$$

$G_{\mu\nu}$ is the Einstein tensor and encodes the curvature of spacetime, while $T_{\mu\nu}$ is the energy-momentum tensor, which contains the information on the density and flux of energy and momentum in spacetime. G is the Newtonian constant of gravitation, and is not related to $G_{\mu\nu}$. Another important quantity is the *metric tensor* $g_{\mu\nu}$, which encapsulates the geometry of spacetime through

$$\mathrm{d}s^2 = g_{\mu\nu} \mathrm{d}x^\mu \mathrm{d}x^\nu \,, \tag{2.2}$$

with $\mathrm{d}s^2$ the spacetime interval and x^μ the coordinate four-vector $(ct, \mathbf{x})$. The Einstein tensor $G_{\mu\nu}$ and the metric $g_{\mu\nu}$ are linked through a complex collection of nonlinear partial differential equations, making the EFE extremely hard to solve by algebraic means. We will thus resort to approximations to derive gravitational-wave propagation and generation. Furthermore, we will introduce the different aspects of a binary black hole coalescence, as well as its detection.

2.1 A note on cosmological distances

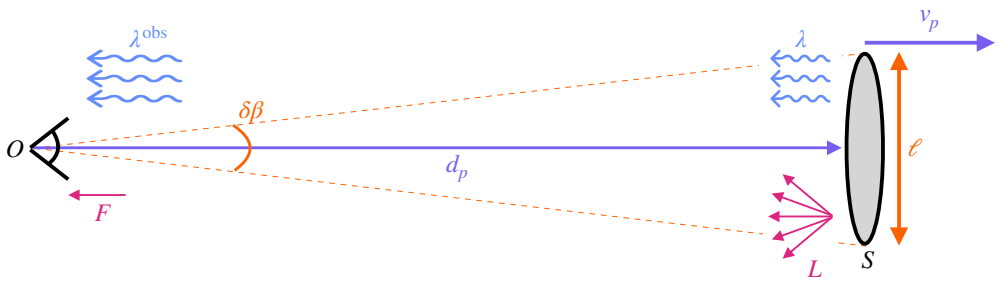

Figure 1: An illustration of a source S moving away from an observer O in an expanding universe. The source is located at proper distance d_p, and is receding with proper velocity v_p due to the expansion of the Universe. It has true size ℓ, radiates at luminosity L and emits wavelengths λ. The observer sees the source with an angular size $\delta\beta$, measures a radiated flux F and detects wavelengths λ_{obs}. These three sets of observables connect to different definitions of distances.

We live in an expanding universe, where binary black hole mergers are expected to occur out to large look-back times[2]. While the gravitational waves travel, the distances between objects changes due to the expansion, and as such our Euclidean notion of 'distance' is no longer unambiguous.

We will thus need to precisely redefine it. In Fig. 1, we see a source S receding from an observer O with proper velocity v_p due to the expansion of the Universe. The source radiates at a luminosity L with wavelengths λ, while having a true size ℓ. The *proper distance* d_p is related to the velocity of the source through Hubble's law: $d_p = H_0 v_p$, where the Hubble constant H_0 quantifies the expansion rate of the Universe. However, there are no straightforward ways of measuring the proper distance or the proper velocity, i.e. we cannot pull out a yardstick and mark the difference between two galaxies. Thus, different distances can be defined, which we will briefly outline in this section.

A radiating source in a static, Euclidean space obeys the inverse-square law: the measured flux F is proportional to the luminosity L divided by the distance squared. In an expanding universe, this relation no longer

[2]The look-back the time is the amount of time a ray of light traveled from its source to us (the observer), and is thus a measure for distance.

holds true, as the distance between source and observer changes over time. The *luminosity distance* d_L is defined such that

$$d_L \equiv \left(\frac{L}{4\pi F}\right)^{1/2}, \tag{2.3}$$

and can be measured when the luminosity of an object is known through other means, a so-called standard candle. The true size of the source ℓ and its apparent angular size $\delta\beta$ are related through the *angular-diameter distance* D

$$D \equiv \frac{\ell}{\delta\beta}, \tag{2.4}$$

which holds true for $\delta\beta \ll 1$. Finally, the proper distance changes over time, as the universe continues to expand. It is thus convenient to define the *comoving distance* r (or D^c), which is defined as the proper distance at the current time t_0. While the relation between the comoving distance, luminosity distance and angular-diameter distance might seem non-existent, the three are actually directly correlated. Due to the expansion of spacetime, the emitted wavelengths λ are altered through the Doppler effect, which defines the *redshift* z as

$$1 + z = \frac{\lambda^{\text{obs}}}{\lambda}, \tag{2.5}$$

where λ^{obs} are the wavelengths as measured by the observer. Redshift is thus a measure of distance as well, since it quantifies the stretching of a yard-stick as it travels from the source to the observer whilst space expands. One can show (see, e.g. [50]) that the relation between these different quantities then becomes

$$(1 + z)D = r = d_p(t = t_0) = \frac{d_L}{1 + z}. \tag{2.6}$$

2.2 Linearised gravity

With these notions of distance cemented, we can get started on the gravitational waves, and derive a formalism for their generation and propagation. We will use the weak-field approximation[3], which is valid at large distances from the BBH merger. This allows us to write

$$g_{\mu\nu} = \eta_{\mu\nu} + h_{\mu\nu}, \tag{2.7}$$

where $\eta_{\mu\nu}$ is the Minkowski metric for special relativity and $|h_{\mu\nu}| << 1$ is a small perturbation with respect to $\eta_{\mu\nu}$. It is this perturbation that will be allowed to vary in time and will contain the gravitational wave. Since the subsequent derivation is not relevant for the remainder of this work, we will only show the result here, but refer the interested reader to Ref. [51]. After working out $G_{\mu\nu}$ for the new metric, we get

$$\Box\bar{h}_{\mu\nu} = \frac{16\pi G}{c^4} T_{\mu\nu}, \tag{2.8}$$

with $\Box = \frac{1}{c^2}\frac{\partial^2}{\partial t^2} - \nabla^2$ the d'Alembertian and $\bar{h}_{\mu\nu} = h_{\mu\nu} - 0.5\eta_{\mu\nu}h$ a symmetric definition of the perturbation with $h = h^\alpha_\alpha$ the trace. This result only holds in the Lorentz gauge, which demands that $\partial^\mu\bar{h}_{\mu\nu} = 0$. A gauge is a set of constraints on top of the already existing physical formulas, designed to remove redundant degrees of freedom in field theories. There is residual gauge freedom in the wave equation (Eq. (2.8)), so we can take the transverse-traceless (TT) gauge when necessary, where $\bar{h}_{0\mu} = 0$ and $\bar{h}^\alpha_\alpha = 0$, without loss of generality. In the vacuum of space, the wave equation reduces to

$$\Box\bar{h}_{\mu\nu} = 0 \tag{2.9}$$

which is the equation for plane wave propagation. Suppose we now have a plane wave traveling in the z-direction. The transverse-traceless gauge ensures that the wave oscillates perpendicular to the direction of propagation, giving

$$h^{TT}_{ij} = \begin{pmatrix} h_+ & h_\times & 0 \\ h_\times & -h_+ & 0 \\ 0 & 0 & 0 \end{pmatrix} \cos(\omega(t - z/c)), \tag{2.10}$$

[3]The weak-field approximation states that weak gravitational fields can be modelled as a superposition of a flat spacetime and a small perturbation.

with h_+ and $h_\times$ the plus and cross polarisations, respectively. The plus polarisation causes space to alternatingly stretch in the x and y direction, while the cross polarisation behaves similarly at an angle of 45° (see Fig 2, for an illustration). The waves travel at the speed of light c, which completes our framework for gravitational-wave propagation.

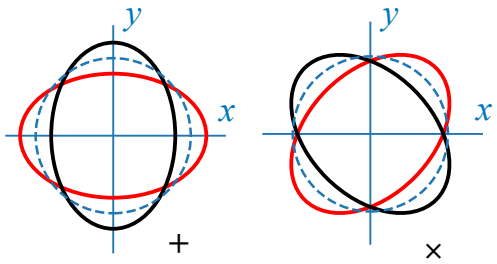

Figure 2: An illustration of the effect of the plus and cross polarisation on a ring (blue dashes). The ring is alternately stretched and compressed along two principle axes, which are rotated at an angle of 45° between the different polarisations. Adapted from [40]

Now that we know how gravitational waves propagate, we can look into their generation. Inspecting the wave equation (Eq. (2.8)), we can identify $T_{\mu\nu}$ as the source of gravitational waves and consequently solve the equation using the appropriate Green's function. We must also take care to move to the transverse-traceless gauge, giving us

$$h_{ij}^{TT}(t,\mathbf{x}) = \frac{4G}{c^4}\Lambda_{ij,kl}(\hat{n})\int_{\mathcal{V}} \mathrm{d}^3\mathbf{x}' \frac{1}{|\mathbf{x}-\mathbf{x}'|}T^{kl}(t-|\mathbf{x}-\mathbf{x}'|/c,\mathbf{x}')\,, \tag{2.11}$$

where $\Lambda_{ij,kl}$ is the projection operator from the Lorentz gauge to the TT gauge, $\hat{n}$ is the unit vector in the direction of propagation and the volume $\mathcal{V}$ is the volume containing the binary black holes. The observer at $\mathbf{x}$ (our detectors) will typically be at a large comoving distance r from the source, so we can approximate $|\mathbf{x}-\mathbf{x}'| \simeq r$, effectively neglecting the inner details of the binary system. This holds well for non-relativistic binaries, and gives us

$$h_{ij}^{TT}(t,\mathbf{x}) = \frac{1}{r}\frac{2G}{c^4}\Lambda_{ij,kl}(\hat{n})\ddot{M}^{kl}(t-r/c)\,, \tag{2.12}$$

with M^{ij} the mass quadrupole moment given by

$$M^{ij}(t') = \frac{1}{c^2}\int_{\mathcal{V}} \mathrm{d}^3\mathbf{x}\; T^{00}(t',\mathbf{x})x^i x^j\,. \tag{2.13}$$

These two equations give us exactly what we want: the gravitational wave in the TT gauge as generated by the energy-mass density T^{00}. Since we are free to choose our coordinate system, we can again take z to be the direction of propagation and get direct expressions for h_+ and $h_\times$:

$$\begin{aligned} h_+ &= \frac{1}{r}\frac{G}{c^4}(\ddot{M}_{11}-\ddot{M}_{22}) \\ h_\times &= \frac{2}{r}\frac{G}{c^4}\ddot{M}_{12}\,, \end{aligned} \tag{2.14}$$

with the quadrupole mass moments evaluated at the retarded time $t_{\mathrm{ret}} = t - r/c$. These are the simplest expressions possible for gravitational waves, and exclude many effects such as higher order terms in mass moments and time derivatives, as well as spins. There exist other formalisms that include more corrections, such as the full Post-Newtonian (PN) expansion (see, e.g. [52]), where Einstein's equations (Eq. (2.1)) are expanded in terms of the typical velocity of the system divided by the speed of light. We will not treat these extensions here, as they do not contribute to the general discussion.

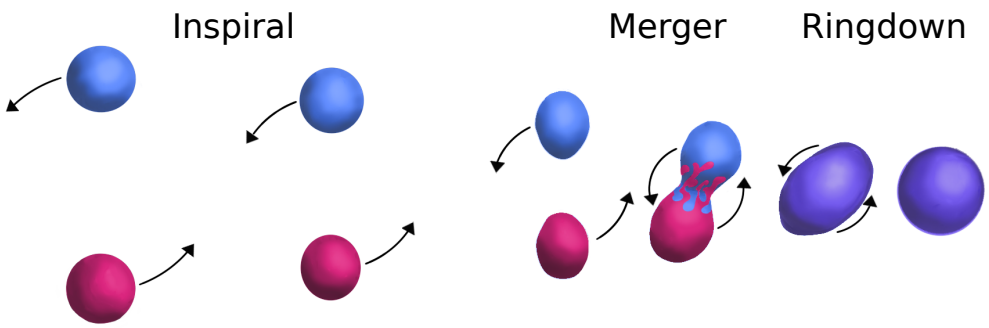

Figure 3: An illustration of the coalescence process, starting with the inspiral on quasi-circular orbits, followed by the plunge and merger, and completed by the ringdown. Personal work.

2.3 A binary black hole coalescence: inspiral, merger and ringdown

We will look into binary black hole (BBH) coalescences, since those are detectable out to high redshifts where lensing can occur, and their population has relatively well constrained properties. Binary neutron stars can emit gravitational waves as well, but are only detectable out to about a hundred Mpc. The small total number of galaxies between us and the neutron stars makes lensing unlikely to occur.

There are three main phases to a BBH coalescence: inspiral, merger and ringdown. We will make approximations to the inspiral phase to derive expressions for the polarisations (Eq. (2.14)) and their frequency evolution, while we will discuss the process of merger and ringdown in a descriptive manner. An illustration of the process is shown in Fig. 3.

We make the approximation that the black holes are on quasi-circular orbits during the inspiral to simplify our equations. We can treat the black holes as point particles with masses m_1 and $m_2 < m_1$ that orbit each other with angular frequency ω. The direction of propagation (towards the observer) is along the z-axis, while the normal to the orbital plane is tilted at the inclination angle ι with respect to the z-axis. Following the derivation in Appendix A.1 for stationary orbits, we get

$$\begin{aligned} h_+ &= -\frac{4}{r}\left(\frac{G\mathcal{M}_c}{c^2}\right)^{5/3}\left(\frac{\omega}{c}\right)^{2/3}\frac{1+\cos^2(\iota)}{2}\cos(2\omega t_{\rm ret}) \\ h_\times &= -\frac{4}{r}\left(\frac{G\mathcal{M}_c}{c^2}\right)^{5/3}\left(\frac{\omega}{c}\right)^{2/3}\cos(\iota)\sin(2\omega t_{\rm ret})\,, \end{aligned} \tag{2.15}$$

where we introduced the *chirp mass*

$$\mathcal{M}_c = \frac{(m_1 m_2)^{3/5}}{(m_1+m_2)^{1/5}}\,. \tag{2.16}$$

While the definition of the chirp mass might seem arbitrary, it plays an important role in the functional form of a gravitational wave. Note that the frequency of the waves is twice the orbital frequency.

Gravitational waves carry energy away from the system since they need it to curve space and time. The energy is taken from the orbital energy of the system, causing the orbits to shrink over time. Through Kepler's third law, we find that the shrinking of orbits increases the orbital frequency. Thus, we write $\omega \to \omega(t_{\rm ret})$ and $\omega t_{\rm ret} \to \Phi(t_{\rm ret})$. The frequency evolution can then be found using conservation of total energy, namely the sum of orbital energy $E_{\rm orb}$ and energy carried away by the gravitational waves $E_{\rm GW}$.

Orbital energy is the combination of classical kinetic energy and gravitational potential energy, which can be written as

$$E_{\rm orb} = -\frac{1}{2}(G^2\mathcal{M}_c^5\omega^2)^{1/3}\,. \tag{2.17}$$

The gravitational-wave energy is derived in Ref. [53], and we will go through an abridged version here. Referring back to the EFE (Eq. (2.1)), we want to separate the energy-momentum tensor $T_{\mu\nu}$ into a background tensor $T^{(B)}_{\mu\nu}$ and the higher-order effect of the gravitational waves. This effect is encapsulated up to quadratic order in $h_{\mu\nu}$ by the effective stress-energy tensor $t_{\mu\nu}$, which is given by

$$t_{\mu\nu} = -\frac{c^4}{32\pi G}\langle \partial_\mu h_{\rho\sigma} \partial_\nu h^{\rho\sigma} \rangle \,, \tag{2.18}$$

where the average is calculated over a region of spacetime large enough to contain several gravitational-wave oscillations. A detailed calculation then shows that the energy passing through a sphere $\mathcal{S}$ of radius r per unit time is given by

$$\frac{\mathrm{d}E_{\mathrm{GW}}}{\mathrm{d}t} = \frac{c^3 r^2}{16\pi G}\int_{\mathcal{S}} \mathrm{d}\Omega \, \langle \dot{h}_+^2 + \dot{h}_\times^2 \rangle \,, \tag{2.19}$$

in terms of the plus and cross polarisations. We can substitute the functional forms of the polarisations (Eq. (2.14), with time-dependence) to get an explicit formula for the energy carried away by gravitational waves

$$\frac{\mathrm{d}E_{\mathrm{GW}}}{\mathrm{d}t} = \frac{32}{5}\frac{c^5}{G}\left(\frac{G\mathcal{M}_c \omega}{c^3}\right)^{10/3} . \tag{2.20}$$

In the following, we will write the energies and polarisations in terms of the gravitational-wave frequency $f_{\mathrm{gw}} = 2f_{\mathrm{orb}}$, such that $\omega = \pi f_{\mathrm{gw}}$. Energy conservation dictates that $\mathrm{d}E_{\mathrm{tot}}/\mathrm{d}t = 0$, which gives us a differential equation in terms of f_{gw} and its time derivative $\dot{f}_{\mathrm{gw}}$. Solving this equation yields

$$f_{\mathrm{gw}}(t) = \frac{1}{\pi}\left(\frac{G\mathcal{M}_c}{c^3}\right)^{-5/8}\left(\frac{5}{256}\frac{1}{\tau(t)}\right)^{3/8} , \tag{2.21}$$

with $\tau(t) = t_c - t$ and t_c the time of coalescence. The most important take-away from Eq. (2.21) is that the frequency evolution of a gravitational wave is entirely governed by the chirp mass, within our approximations. It is convenient to write these results in terms of the time t^{obs} and the redshifted frequency $f^{\mathrm{obs}}_{\mathrm{gw}}$ at the observer instead of the source. This gives us our final result for the simplified inspiral phase of the gravitational wave waveform

$$\begin{aligned} h_+ &= -\frac{4}{d_L}\left(\frac{G\mathcal{M}_z}{c^2}\right)^{5/3}\left(\frac{\pi f^{\mathrm{obs}}_{\mathrm{gw}}(t^{\mathrm{obs}}_{\mathrm{ret}})}{c}\right)^{2/3}\frac{1+\cos^2(\iota)}{2}\cos\big(\Phi_{\mathrm{gw}}(t^{\mathrm{obs}}_{\mathrm{ret}})\big) \\ h_\times &= -\frac{4}{d_L}\left(\frac{G\mathcal{M}_z}{c^2}\right)^{5/3}\left(\frac{\pi f^{\mathrm{obs}}_{\mathrm{gw}}(t^{\mathrm{obs}}_{\mathrm{ret}})}{c}\right)^{2/3}\cos(\iota)\sin\big(\Phi_{\mathrm{gw}}(t^{\mathrm{obs}}_{\mathrm{ret}})\big) \,, \end{aligned} \tag{2.22}$$

with d_L the luminosity distance to the source and $\mathcal{M}_z = (1+z)\mathcal{M}_c$ the redshifted chirp mass.

In the current situation, the frequency goes to infinity as $t \to t_c$. However, our approximations become invalid at small orbits, where the curvature of the background metric is no longer negligible, and the full Post-Newtonian expansion becomes a more appropriate approximation. After working out the details [54], we find the existence of an *innermost stable circular orbit* (ISCO) at a separation of $R_{\mathrm{ISCO}} = 6GM/c^2$, which separates the inspiral from the merger phase. Using Kepler's third law, we find that this corresponds to a gravitational wave frequency

$$f^{\mathrm{obs}}_{\mathrm{gw,ISCO}} = \frac{c^3}{6^{3/2}\pi GM(1+z)} \,, \tag{2.23}$$

where M is the total mass of the system $m_1 + m_2$. Furthermore, the PN formalism is commonly used to calculate the accurate inspiral waveforms, as it includes individual component masses and spins into the polarisations. So while we derived functional forms for the polarisations and their frequency evolution, it is important to take note of these caveats.

When the binary black holes cross the innermost stable circular orbit, they start to plummet towards each other and go into the merger phase. This is a rather violent process that takes place in the strong gravity field

regime, so the full machinery of general relativity is needed. In large numerical simulations, the solutions to Eq. (2.1) are calculated and evolved through time to solve for the merger (see, e.g. [55]).

When the two binary black holes have merged together, they form a single excited black hole. This will then settle into a dormant state, shedding its spherical asymmetry in the form of gravitational waves. Their form can be derived in a perturbative setting, but numerical simulation can be applied as well. Altogether, a few solar masses of energy are expelled during the entire coalescence in the form of gravitational waves, making binary black hole coalescences one of the brightest events in the Universe in terms of energy flux.

2.4 Gravitational wave detection

Gravitational waves periodically stretch space in two different directions, and it is this stretching that we can measure using *laser interferometers*. A monochromatic laser with a very well defined wavelength is shot towards a beam splitter. Here, 50% of the light is let through, whereas the other 50% is deflected at right angles. Both beams now travel through arms several kilometers long, 4 km in the LIGO detectors and 3 km in the Virgo detector. They are reflected back at the end of each arm, travel up and down the two arms about 300 times, and finally combine back together at the beam splitter (see Fig. 5 for an illustration). This set-up can be tuned to make sure that destructive interference takes place when no gravitational wave is passing, giving an output of zero. When a gravitational wave passes through the interferometer, stretching of space will then change the lengths of the arms independently, and the destructive interference is lifted to give rise to a signal.

The response of each arm depends on the location and orientation of the source in the sky, relative to the detector (see Fig. 4). The total response $h(t)$ can then be characterised by

$$h(t) = F_+(\theta, \phi, \psi)h_+(t) + F_\times(\theta, \phi, \psi)h_\times(t)\,, \tag{2.24}$$

where θ, ϕ and ψ are the angles characterising the orientation of the source with respect to the interferometer,

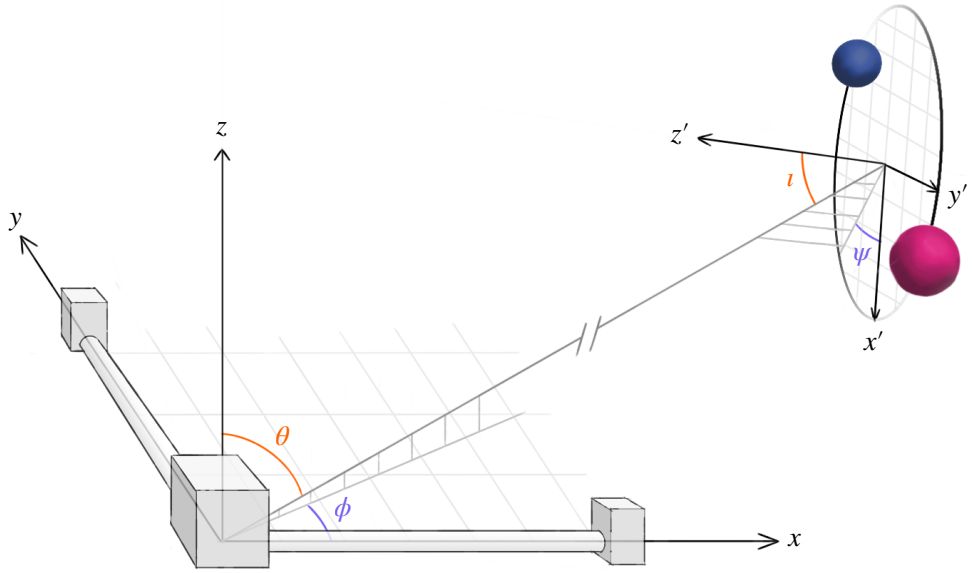

Figure 4: An illustration of the detector frame and the source frame, together with their associated angles connecting them through the line-of-sight. In the detector frame, the angles θ and ϕ give the sky position, while the angles ι (inclination) and ψ (polarisation) give the relative orientation of the orbital plane with respect to the line-of-sight. Not to scale.

and F_+ and $F_\times$ are the so called *beam pattern functions*:

$$F_+(\theta,\phi,\psi) = \frac{1}{2}(1+\cos^2(\theta))\cos(2\phi)\cos(2\psi) - \cos(\theta)\sin(2\phi)\sin(2\psi)$$
$$F_\times(\theta,\phi,\psi) = \frac{1}{2}(1+\cos^2(\theta))\cos(2\phi)\sin(2\psi) + \cos(\theta)\sin(2\phi)\cos(2\psi)\,. \tag{2.25}$$

Note that the definitions of θ and ϕ change over time relative to fixed points on the sky, since the orientation of the detectors changes with the rotation of the Earth. This allows us to express the beam pattern functions as functions of the right ascension α, the declination δ, the time of arrival t_{arrival} and the polarisation ψ.

The beam pattern functions characterise the response of the detector to the plus and cross polarisations. Imagine a source directly overhead the detector in Fig. 4, along the z-axis. The cross polarisation will stretch the two detector arms an equal amount, rendering the detector insensitive to this polarisation as it only registers relative differences between the lengths of the arms. The plus polarisation is co-aligned in this scenario, and will incite a large detector response. The beam pattern functions are the quantification of this effect, generalised for all orientations.

Inspecting the polarisations (Eq. (2.15)), we note that both have a factor h_0 in their amplitude. This allows us to simplify the total response (Eq. (2.24)) to [56]

$$h(t) = A(\iota,\psi,\alpha,\delta,t_{\text{arrival}})h_0\cos(\Phi_{\text{gw}}(t)-\Phi_0) \tag{2.26}$$

where $\Phi_{\text{gw}}(t) = 2\pi t_{\text{ret}} f_{\text{gw}}(t_{\text{ret}})$ and A the *antenna pattern* given by:

$$A = (A_+^2 + A_\times^2)^{1/2}\,, \quad \tan(\Phi_0) = \frac{A_+}{A_\times}\,, \quad A_+ = \frac{1+\cos^2(\iota)}{2}F_+\,, \quad A_\times = \cos(\iota)F_\times\,. \tag{2.27}$$

We now have an expression for $h(t)$, but sadly there is a lot of noise to be dealt with in the detector. Tectonic plates are constantly on the move, the mirrors experience thermal vibrations, and the photodiode experiences shot noise, for example [14]. With the inclusion of noise, the detector data strain then becomes

$$s(t) = h(t) + n(t)\,, \tag{2.28}$$

with $n(t)$ the noise in the detector at time t. Some of this noise can be filtered out by figuring out what the sources are and correcting for it, but we need a more precise method to dig up gravitational waves. One such method is *matched filtering*. Presume you expect a signal from a binary with masses m_1 and m_2. From the discussion in Sec. 2.3, we know that the frequency evolution is mostly governed by the chirp mass, which in turn determines most of the functional form of the gravitational wave. We can thus construct a template for the expected response $h(t)$, and check the match between the strain s and the template at each moment in time in the data. Doing so allows us to detect gravitational waves with greater efficiency.

We define a detection statistic to quantify the match between the strain and the template, called the *signal-to-noise ratio* (SNR) ρ:

$$\rho = \frac{(h|s)}{(h|h)^{1/2}}\,, \text{ with } (A|B) \equiv 4\text{Re}\int_0^\infty \mathrm{d}f\, \frac{\tilde{A}^*(f)\tilde{B}(f)}{S_n(f)}\,, \tag{2.29}$$

where $S_n(f)$ is the *power spectral density* (PSD) (see the inset in Fig. 5 for an example), which characterises the strength of the noise at frequency f [51]. $(A|B)$ is an inner product involving the Fourier transforms of the functions $A(t)$ and $B(t)$, so this formula is similar to calculating the component of a vector s parallel to the normed vector $\hat{h} = h/||h||$, which is indeed a nice quantification of the match between two vectors. The optimal value of the SNR is attained when $s = h$ and we get $\rho_{\text{opt}} = (h|h)^{1/2}$.

We can now search the entire data strain with a single template and compute the match. However, in reality we do not know what waveforms h to expect. We thus need to search the data with all the possible waveforms. This warrants the construction of a *template bank*. A template bank is a set of templates which attempts to

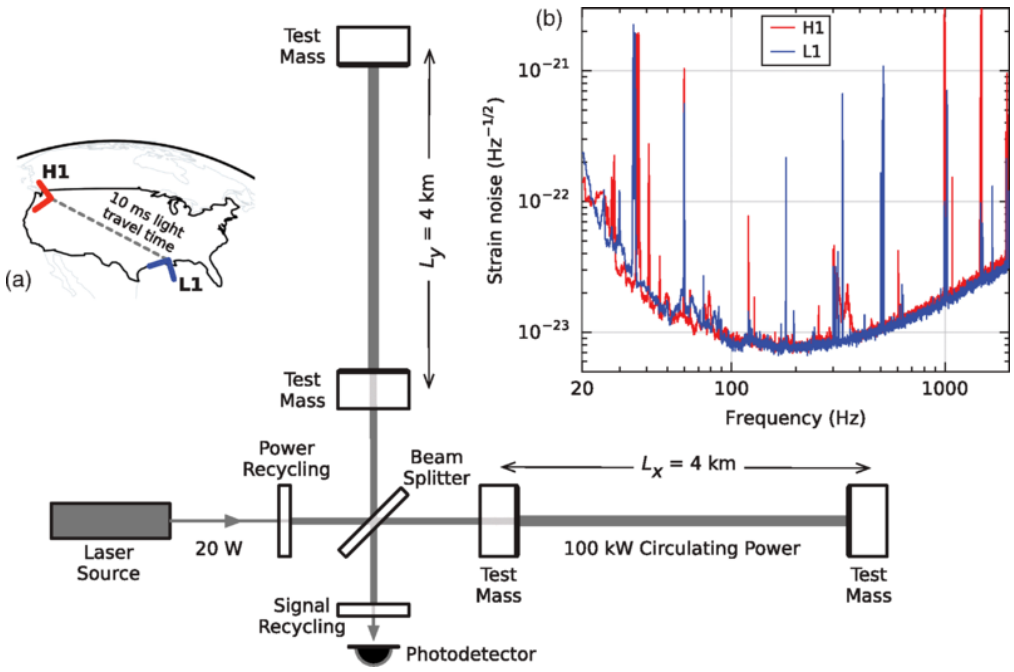

Figure 5: An illustration of the LIGO detectors. Inset (a) shows the relative orientations of the Livingston (L1) and Hanford (H1) detectors, while inset (b) shows the noise in both the detectors at the time of detection of GW150914. From [14].

cover the expected (m_1, m_2)-space as efficiently as possible. For high chirp masses, $f_{\rm ISCO}$ is quite low and the wave is visible in the detector for only a few waveform cycles, so the templates do not have to match precisely to give a high SNR. Lower chirp masses are observable for longer time periods, and the templates need to be more densely packed. In a search, all of the templates are continuously slid across the data strain, recording which templates give what SNR at all times.

We have now mostly dealt with noise, but there is still the possibility of a glitch appearing in a detector, mimicking a gravitational wave. We can quantify how likely a glitch is to produce a certain SNR, and construct a probability distribution $p(\rho)$. If we then observe a trigger with an SNR of ρ^*, the survival function of $p(\rho)$ (one minus the cumulative distribution) at $\rho = \rho^*$ tells us the probability of glitches giving an equal or higher SNR. Typically, detection triggers with an SNR ≥ 8 are considered good candidates for astrophysical events [57], and thus we will adopt an SNR ≥ 8 as the detection threshold in this work.

2.5 The observed event rate

One of the goals of this work is to predict the number of observed events within LIGO-Virgo-KAGRA. The number of expected gravitational-wave events per year can be expressed as an integral over the comoving volume $V_c = \frac{4}{3}\pi r^3$

$$\frac{{\rm d}N}{{\rm d}t} = \int \frac{{\rm d}N}{{\rm d}V_c {\rm d}t} \frac{{\rm d}V_c}{{\rm d}z_s} {\rm d}z_s \,, \tag{2.30}$$

where ${\rm d}N/({\rm d}V_c{\rm d}t)$ is the merger-rate density measured in the detector frame, ${\rm d}V_c/{\rm d}z_s$ is the differential comoving volume, and z_s is the redshift of the source binary black hole merger. The output of theoretical predictions and observational papers is the merger-rate density measured in the source frame $\mathcal{R}(z_s) = {\rm d}N/({\rm d}V_c{\rm d}t_s) = (1+z_s)[{\rm d}N/({\rm d}V_c{\rm d}t)]$. Therefore, we express the integral in terms of the merger-rate density in the source frame

$$\frac{{\rm d}N}{{\rm d}t} = \int \frac{\mathcal{R}(z_s)}{1+z_s} \frac{{\rm d}V_c}{{\rm d}z_s} {\rm d}z_s \,. \tag{2.31}$$

On the other hand, not all mergers are observed within LIGO-Virgo-KAGRA. Instead, only a fraction of signals at redshift z_s with an SNR larger than some detection SNR threshold ρ_c are observed

$$P(\rho > \rho_c|z_s) = \int \Theta(\rho(z_s, \boldsymbol{\theta}) - \rho_c) p(\boldsymbol{\theta}) d\boldsymbol{\theta}\,, \tag{2.32}$$

where $\rho(z_s, \boldsymbol{\theta})$ is the SNR of a signal with parameters of the binary black hole system $\boldsymbol{\theta}$, $\Theta(\rho(z_s, \boldsymbol{\theta}) - \rho_c)$ is the heaviside theta function, and $p(\boldsymbol{\theta})$ is the distribution of the binary parameters. Therefore, the rate of *observed* mergers is

$$\frac{\mathrm{d}N_{\mathrm{obs}}}{\mathrm{d}t} = \int \frac{\mathcal{R}(z_s)}{1+z_s} \Theta(\rho(z_s, \boldsymbol{\theta}) - \rho_c) \frac{\mathrm{d}V_c}{\mathrm{d}z_s} p(\boldsymbol{\theta}) \mathrm{d}\boldsymbol{\theta} \mathrm{d}z_s\,. \tag{2.33}$$

The observed rate is sensitive to the merger-rate density $\mathcal{R}(z_s)$, as well as assumptions on the population of binary black holes $p(\boldsymbol{\theta})$. This is the first step in predicting the rate of observed lensed mergers, which we will work towards in the next section.

3 Gravitational lensing

We can now adequately describe gravitational waves, so the next topic to be covered is gravitational lensing. Both light and gravitational waves follow the same paths in space, called null geodesics. In a flat Minkowski spacetime, these are just straight lines, but they become increasingly complicated for arbitrarily curved spacetimes. Luckily, most of space is empty and can be described by the background metric, such as the Friedmann-Lemaître-Robertson-Walker (FLRW) metric. This metric can be approximated as locally flat, while being curved at larger scales. Gravitational lensing requires the waves to pass by sufficiently close to a galaxy or galaxy cluster, to within its area of effect on the local metric. However, these lenses have a sufficiently weak Newtonian gravitational potential $|\Phi| << c^2$, such that they can be treated as only weakly perturbing the FLRW metric.

3.1 The effects of lensing and the lens equation[4]

There are three stages to the journey of a lensed gravitational wave. First, the wave travels from the source to the lens in a FLRW metric. Secondly, the wave is deflected by the lens in an approximately flat metric weakly perturbed by a gravitational potential. Finally, the wave propagates once more in a FLRW metric from the lens to the observer. Stage two takes place at sufficiently small scales compared to stage one and three, such that we can treat the lens in the thin-lens approximation. Furthermore, we take the lens size to be much larger than the wavelength of the gravitational wave, which allows us to work in the geometrical optics limit, essentially rendering the lens achromatic [21].

Fig. 6 shows the geometry of a lensed system consisting of a source S, a lens L and an observer O. Gravitational waves travel from the source to $\vec{\xi}$, where they get deflected by an angle $\hat{\alpha}$. The observer then sees the image S' at angular position $\vec{\theta}$, while the original source has angular position $\vec{\beta}$. The distances are angular diameter distances, such that separation = angle × distance, and they are a function of the source redshift z_s and the lens redshift z_L. This allows us to write the change in separation

$$\vec{\eta}' - \vec{\eta} = D_S\vec{\theta} - D_S\vec{\beta} = D_{LS}\hat{\alpha}\,, \tag{3.1}$$

for small deflections $\hat{\alpha}$. From Fig. 6, we conclude that $D_{LS}\hat{\alpha} = D_S\vec{\alpha}$, where $\vec{\alpha}$ is the reduced deflection angle. This gives us the *lens equation*

$$\vec{\beta} = \vec{\theta} - \vec{\alpha}(\vec{\theta})\,, \tag{3.2}$$

which relates the source position $\vec{\beta}$ to the image positions $\vec{\theta}$. This is a generally nonlinear equation, and it can have *multiple solutions* for a single source position.

[4] This section was inspired by Ref. [58]

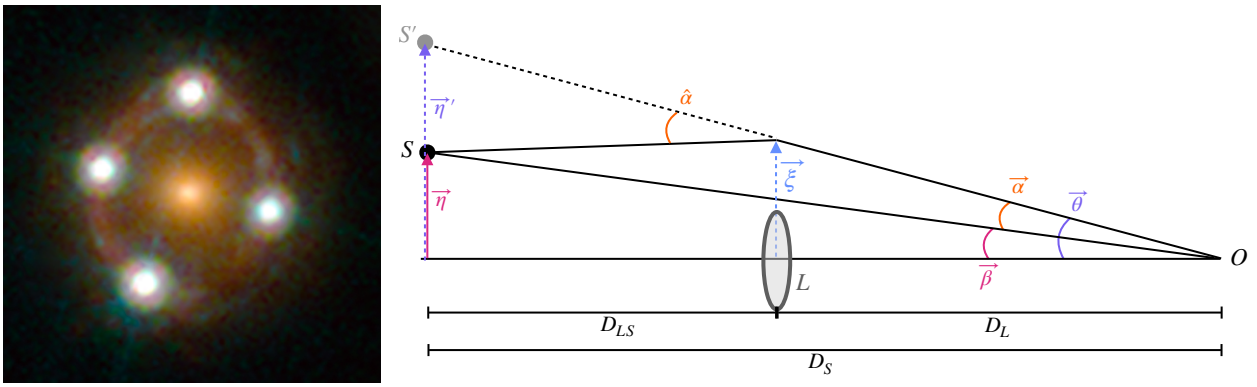

Figure 6: *Left*: The strongly lensed quasar HE0435-1223. The foreground galaxy at the centre of the image curves the light from the distant quasar, which we observe as four distinct images. Credits: ESA/Hubble, NASA, Suyu et al. *Right*: An illustrative lensed configuration consisting of a source S, image S', lens L and observer O. All angles and vectors are with respect to an arbitrary optical axis, which we have chosen through the centre of the lens for convenience. The vectors $\vec{\eta}$, $\vec{\eta}'$ and $\vec{\xi}$ are all 2D, the latter lying in the lens plane while the other two lie in the source plane. The angles $\hat{\alpha}$, $\vec{\alpha}$, $\vec{\beta}$ and $\vec{\theta}$ are all small, such that he distances D_S, D_L and D_{LS} are the angular diameter distances between OS, OL, and LS, respectively. Configurations with multiple images are possible, but not shown here. Not to scale.

Our big unknown is the deflection $\vec{\alpha}$, which depends on the properties of the lens. We treat the lens in the Newtonian limit, where it has a gravitational potential $\Phi(\vec{r})$. For small deflections, $\hat{\alpha}$ is given by

$$\hat{\alpha} = \frac{2}{c^2} \int \vec{\nabla}_\perp \Phi \, \mathrm{d}z \,, \tag{3.3}$$

with $\vec{\nabla}_\perp$ the gradient perpendicular to z. The depth of the lens is negligible with respect to the distances D_L, D_S and D_{LS}, so we can define a scaled 2D projection of Φ:

$$\psi(\vec{\theta}) = \frac{D_{LS}}{D_L D_S} \frac{2}{c^2} \int \Phi(D_L \vec{\theta}, z) \, \mathrm{d}z \,. \tag{3.4}$$

We then retrieve a simple relation between the scaled potential ψ and the reduced deflection angle $\vec{\alpha}$

$$\vec{\nabla}_{\vec{\theta}} \psi = \vec{\alpha} \,, \tag{3.5}$$

where $\vec{\nabla}_{\vec{\theta}}$ is the gradient with respect to $\vec{\theta}$. More properties of the lens effects are incorporated in the Jacobian matrix $\mathcal{A}$

$$\mathcal{A}_{jk}(\vec{\theta}) \equiv \frac{\partial \beta_j(\vec{\theta})}{\partial \theta_k} = \left(\delta_{jk} - \frac{\partial^2 \psi(\vec{\theta})}{\partial \theta_j \partial \theta_k} \right) \,, \tag{3.6}$$

where the second equality follows from plugging in the lens equation (Eq. (3.2)) and the reduced deflection angle (Eq. (3.5)). This Jacobian describes the mapping of $\mathrm{d}\vec{\theta}$ to $\mathrm{d}\vec{\beta}$ and is called the inverse magnification tensor. The magnification μ of the j-th image itself is given by

$$\mu_j = \frac{1}{\det \, \mathcal{A}(\vec{\theta_j})} \,, \tag{3.7}$$

which physically is the ratio between a solid-angle element $\delta\beta^2$ of the source and its corresponding solid-angle element $\delta\theta^2$ of the image, for finitely sized sources. The apparent size of lensed sources is thus altered by the magnification, and the measured flux is enhanced by exactly the absolute value of the magnification. We can rewrite the lens equation (Eq. (3.2)), such that

$$\vec{\nabla}_{\vec{\theta}} \left[\frac{1}{2} (\vec{\theta} - \vec{\beta})^2 - \psi(\vec{\theta}) \right] = 0 \,, \tag{3.8}$$

by plugging in the definition for $\vec{\alpha}$ (Eq. (3.5)) and writing the result as a gradient. This equation can then easily be linked to the *time-delay function* [59]

$$t_d(\vec{\theta}) = \frac{1+z_L}{c}\frac{D_L D_S}{D_{LS}}\left[\frac{1}{2}(\vec{\theta}-\vec{\beta})^2 - \psi(\vec{\theta})\right] \\ = t_{\text{geometric}} + t_{\text{gravity}}\,, \tag{3.9}$$

where $t_{\text{geometric}}$ is the time-delay due to the extra length of the deflected light path as opposed to the unlensed case, and t_{gravity} comes from the curvature of spacetime. The time-delay function gives the difference in arrival time between a curved path through a gravitational potential and a path through a flat spacetime, given a specific source-lens configuration.

Altogether, the lens equation has now been reduced to $\vec{\nabla}_{\vec{\theta}}\, t_d(\vec{\theta}) = 0$, which is also known as Fermat's Principle. This states that the path taken by a light-like ray between two given points, is the path that is stationary with respect to variations of said path. The solutions $\vec{\theta}_j$ to the lens equation are called images (see, e.g. Fig. 6) and are thus either minima, saddle points or maxima of the time-delay surface.

The images are categorised by image type, which classifies whether an image corresponds to a minimum (Type I), saddle point (Type II) or a maximum (Type III). These classifications can be made based on the Hessian matrix $\mathcal{T}$ of the time-delay function, which is proportional to the matrix $\mathcal{A}$. Two positive eigenvalues correspond to a minimum, one positive and one negative describes a saddle point and two negative eigenvalues give rise to a maximum. For a light profile, the image gets inverted along one principal axis at a saddle point, while it gets inverted along both axes at a maximum. The lensed gravitational waves acquire a phase shift (the Morse phase), given by $\pi/2$ times the number of negative eigenvalues n_j.

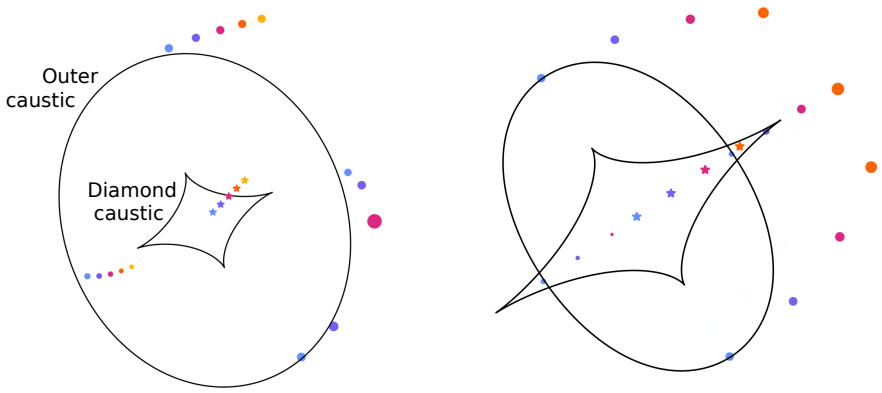

Figure 7: Two different elliptical lenses, with sources shown as stars and their respective images shown as dots in corresponding colours, scaled to their magnification. The lens on the left has a small ellipticity, and shows quadruply lensed (blue, purple), triply lensed (pink) and doubly lensed (orange, yellow) configurations. The lens on the right is highly elliptic, and has a diamond caustic that extends beyond the outer caustic. Its triply lensed configuration (orange) is thus different in nature than the triply lensed system on the left.

The number of images per type follows a specific formula, namely

$$n_{\text{I}} + n_{\text{III}} - n_{\text{II}} = 1\,, \tag{3.10}$$

with $n_{\text{I,II,III}}$ the number of images of Type I, II or III respectively. Fig. 7 shows a number of source and image positions for two different lens configurations. The black lines in the figure are *caustics*, lines in the source plane that separate regions of different image multiplicity. There is always at least one Type I image present, but on its own it counts as weakly lensed. An extra saddle point and maximum appear when crossing over the outer caustic, but the Type III is usually heavily demagnified, and the system is counted as *doubly* lensed. An extra minimum and saddle point come into existence when crossing over into the diamond caustic,

making a *quadruply* lensed system. If the type III image is resolvable, we get the rarer *triply* and *quintuply* lensed systems, respectively. A final possibility is the combination of two Type Is (minima) and a single Type II (saddle point) image, which would give rise to a different kind of triply lensed event (see Fig. 7, orange configuration on the right).

This concludes all of the effects of lensing in the geometrical optics limit: each image comes with a magnification, time-delay and Morse phase. In this work, we will focus on *strong lensing*, where two or more images are formed. In terms of the polarisations (e.g. Eq (2.14)), this translates to a *lensed* waveform [22]

$$\tilde{h}^L_{+,\times}(f,\mathbf{x}) = \sum_j |\mu_j|^{1/2} \tilde{h}_{+,\times}(f,\mathbf{x}) e^{2\pi i f t_{d,j} - i\pi n_j \operatorname{sgn}(f)/2}\,, \tag{3.11}$$

where j sums over all of the images. The polarisations get magnified by the square root of the magnification μ_j, such that their flux is magnified by μ_j itself. Each image receives a different time-delay $t_{d,j}$, essentially changing their respective arrival times, and an overall shift in complex phase due to the Morse phase.

Note that only the magnification has an effect on the optimal SNR ρ_{opt}, the time-delay and the Morse phase are cancelled by the complex conjugate. This also causes a degeneracy between distance and magnification, making the need for multiple images apparent: there is no way to tell whether a single event was lensed or just occurred close by, at least not when only mass quadrupole modes are present.

3.2 Galaxy lenses

Before we can model gravitational-wave lensing, we need to understand the objects that lens them. The two most commong types of astrophysical objects that can cause lensing are galaxies and galaxy clusters. We will focus on galaxies here, but will briefly discuss galaxy clusters towards the end of this section.

We need to know the specific form of the potential ψ (Eq. (3.4)) to find the images of a configuration. This requires us to find a comprehensive set of parameters that optimally describe a galaxy, a so-called galaxy lens model. The simplest model is the Singular Isothermal Sphere (SIS) (see Fig. 8, left illustration). This assumes that the stars in the galaxy behave like an ideal gas, bound by their combined spherically symmetric gravitational potential. The galaxy is assumed to be in thermal equilibrium, such that

$$k_B T = m\sigma_v^2\,, \tag{3.12}$$

with m the mass of the stars and σ_v the one-dimensional *velocity dispersion* of the stars, which is constant for an isothermal stellar gas. We can then require hydrostatic equilibrium

$$\frac{\mathrm{d}p}{\mathrm{d}r} = -\frac{GM(r)\rho(r)}{r^2}\,, \quad \frac{\mathrm{d}M}{\mathrm{d}r} = 4\pi r^2 \rho(r)\,, \tag{3.13}$$

where $M(r)$ is the mass out to a radius r and $\rho(r)$ is the density at r. The equation for hydrostatic equilibrium has a simple solution when combined with thermal equilibrium (Eq. (3.12)) and the ideal gas law, namely

$$\rho(r) = \frac{\sigma_v^2}{2\pi G}\frac{1}{r^2}\,. \tag{3.14}$$

This describes precisely a singular isothermal sphere. For spherically symmetric lenses, sources at $\vec{\beta} = 0$ are mapped to a ring called the Einstein ring. The size of this ring differs between lens models, and for the SIS it is given by

$$\theta_E = \frac{4\pi\sigma_v^2}{c^2}\frac{D_{LS}}{D_S}\,, \tag{3.15}$$

with θ_E the Einstein radius. It contains information on both the size as well as the distances between source, lens and observer, and gives an effective radius within which strong lensing occurs. This concludes the SIS model, which thus has unique parameters σ_v and z_L, given a certain source at redshift z_s.

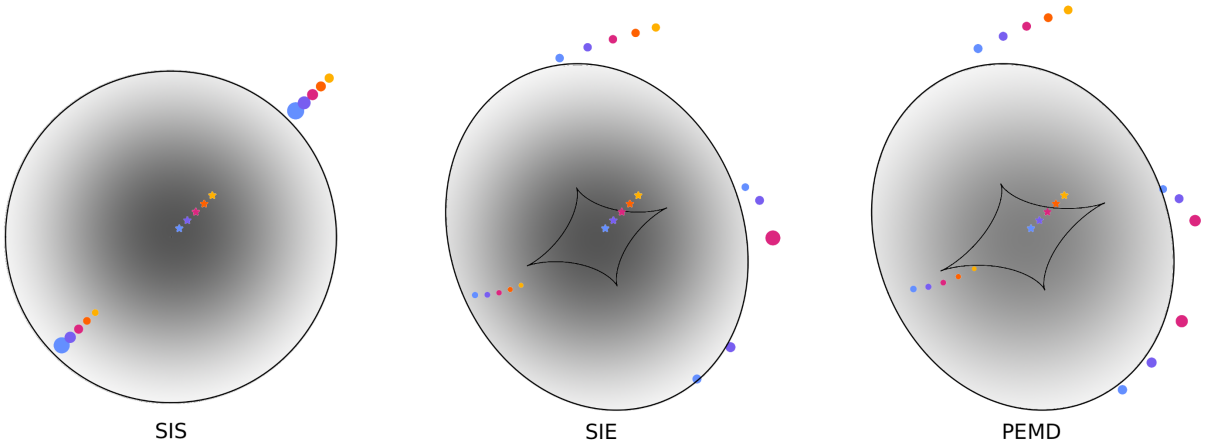

Figure 8: Different lens models with source (stars) and image positions (dots) in corresponding colours, where the grey-scale gradient represent the density distribution. From left to right, we show the Singular Isothermal Sphere (SIS), the Singular Isothermal Ellipsoid (SIE) and the Power-law Ellipse Mass Density profile (PEMD). Four images can only form in elliptical models, while changes to the slope of the density distribution mostly affect the size of the diamond caustic.

All real galaxies are elliptical to some extent, so a correction of the SIS model is the Singular Isothermal Ellipsoid (SIE), which adds an elliptical deformation to the 2D projected density $\Sigma(\vec{\xi}) = \int \rho(\mathbf{r})\mathrm{d}z$ (see Fig. 8, middle illustration). This adds two more parameters: the axis ratio q, which is the ratio between the semi-minor and the semi-major axes, and the orientation ϕ_q of the semi-major axis with respect to the observer's x-axis. The asymmetry of this model allows for the production of quadruple image configurations, whose importance we will discuss later.

The Power-law Ellipse Mass Density profile (PEMD) model allows the power law of the density ρ to vary as well, changing from $\rho \propto r^{-2}$ to $\rho \propto r^{-\gamma}$ (see Fig. 8, right illustration). A point mass would have $\gamma = 3$, while a mass sheet has $\gamma = 1$. The final evolution of these models is the Softened Power law Ellipse Mass Density profile (SPEMD) model, which smoothens out the singularity in the density at the core. This smoothening mostly affects possible 5th images, which we rarely observe, so we will use the PEMD model in this work.

One final addition is the inclusion of an external shear, which adds another elliptical deformation to the lensing potential. While the effect is similar to the ellipticity, it is caused by the surroundings of the galaxy and should thus be modelled separately. Altogether, we now have a set of parameters that completely describe a galaxy lens at redshift z_L: the velocity dispersion σ_v, the axis ratio q and its orientation ϕ_q, the slope of the power law γ, and the two-component shear $\vec{\gamma} = (\gamma_1, \gamma_2)$. This is commonly considered to be a relatively realistic lens model for the purpose of doing lensing statistics with mock data.

Galaxy clusters can also lens sources behind them, but their lens modelling is more complicated. Since they are essentially a collection of moving galaxies, the complexity of the model increases drastically and more approximations are needed. Another option is the use of hydrodynamical simulations (e.g. [60]), but those cannot be translated to lens models straightforwardly. We will thus restrict ourselves to galaxy lensing only, in order to make meaningful predictions.

3.3 The observed lensed event rate

The lensed event rate follows the same idea as in Sec. 2.5, except that 1) only a fraction of of gravitational waves are lensed, and 2) the events can be multiply imaged and magnified. This essentially translates to a change of the merger-rate density in Eq. (2.30)

$$\frac{\mathrm{d}N}{\mathrm{d}V_c\mathrm{d}t} \to \frac{\mathrm{d}N^{\mathrm{SL}}_{\mathrm{obs}}}{\mathrm{d}V_c\mathrm{d}t} = \frac{\mathrm{d}N^{\mathrm{SL}}_{\mathrm{obs}}}{\mathrm{d}N}\frac{\mathrm{d}N}{\mathrm{d}V_c\mathrm{d}t} \tag{3.16}$$

where $\mathrm{d}N^{\mathrm{SL}}_{\mathrm{obs}}/\mathrm{d}N$ is the fraction of observed images from lensed events with respect to total events N. It is composed of the probability that a source at redshift z_s is lensed, times the number of detected images

$$\frac{\mathrm{d}N^{\mathrm{SL}}_{\mathrm{obs}}}{\mathrm{d}N} = \int \left(\sum_j^{\mathrm{images}} \Theta(\rho_j(\boldsymbol{\theta}, z_s, z_L, \boldsymbol{\theta}_L, \vec{\beta}) - \rho_c) \right) \times p(\mathrm{SL}, \boldsymbol{\theta}_L, z_L, \vec{\beta}|z_s) p(\boldsymbol{\theta}) \mathrm{d}\boldsymbol{\theta} \mathrm{d}\boldsymbol{\theta}_L \mathrm{d}z_L \mathrm{d}\vec{\beta}\,,$$

with μ_j and Δt_j the j-th magnification and time-delay of a source at redshift z_s due to a lens at redshift z_L, with lens parameters $\boldsymbol{\theta}_L$ and source position in the lens plane $\vec{\beta}$. The sum enforces detectability of the individual images, while $p(\mathrm{SL}, \boldsymbol{\theta}_L, z_L, \vec{\beta}|z_s)$ represents the fraction of lenses at redshift z_L with parameters $\boldsymbol{\theta}_L$ that strongly lens a source at a given redshift $z_s > z_L$ for a source position in the lens plane $\vec{\beta}$.

We can use Bayes' theorem to further break the probabilities in Eq. (3.17) as follows

$$p(\mathrm{SL}, \boldsymbol{\theta}_L, z_L, \vec{\beta}|z_s) = \tau(z_s) p(\boldsymbol{\theta}_L, z_L, \vec{\beta}|\mathrm{SL}, z_s)\,, \tag{3.17}$$

where we introduced the optical depth $\tau(z_s) = p(\mathrm{SL}|z_s)$, which gives the probability that a source at z_s passes by a galaxy that strongly lenses its signal. We assume $\vec{\beta}$ to be independent of z_s, z_L and $\boldsymbol{\theta}_L$, allowing us to write $p(\boldsymbol{\theta}_L, z_L, \vec{\beta}|\mathrm{SL}, z_s) = p(\boldsymbol{\theta}_L, z_L|\mathrm{SL}, z_s) p(\vec{\beta}|\mathrm{SL})$. Altogether, this gives us the observed lensed image rate in terms of the source frame merger rate density

$$R_{\mathrm{SL}} = \int \frac{\mathcal{R}(z_s)}{1+z_s} \tau(z_s) \left(\sum_j^{\mathrm{images}} \Theta(\rho_j(\boldsymbol{\theta}, z_s, z_L, \boldsymbol{\theta}_L, \vec{\beta}) - \rho_c) p(\boldsymbol{\theta}) \right) \times p(\boldsymbol{\theta}_L, z_L|\mathrm{SL}, z_s) p(\vec{\beta}|\mathrm{SL}) \frac{\mathrm{d}V_c}{\mathrm{d}z_s} \mathrm{d}\boldsymbol{\theta} \mathrm{d}\vec{\beta} \mathrm{d}z_l \mathrm{d}\boldsymbol{\theta}_L \mathrm{d}z_s\,. \tag{3.18}$$

This essentially adds dependencies on the optical depth $\tau(z_s)$ and the strong-lensing galaxy population $p(\boldsymbol{\theta}_L, z_L|\mathrm{SL}, z_s)$ to the observed event rate from Eq. (2.33).

4 The catalogue

As we now have all the necessary theoretical understanding of gravitational waves and the effect of lensing, we will now present the methodology required for modelling the binary black hole and galaxy lens populations. We will use Monte-Carlo integration with importance sampling to solve the integral in Eq. (3.18). This method postulates that

$$\int f(x) p(x) dx \approx \frac{1}{N} \sum_{x_i \text{ from } p(x)} f(x_i)\,, \tag{4.1}$$

for a large number of samples N, where $f(x)$ is a function and $p(x)$ is a probability distribution. The observed lensed event rate can thus be calculated by sampling from the respective probability distributions. We will use this approach to sample all of the parameters in Eq. (3.18) for one million systems. Effectively, this means we will create a population of 10^6 binary black holes, and assign lenses to each of them to create a strong lensing configuration. We will explain these steps in Secs 4.1 and 4.2 respectively.

4.1 The binary black hole population

The parameters that define a binary black hole merger are: source frame masses m_1 and m_2, orbital plane inclination ι and polarisation ψ, redshift z_s, sky localisation (α, δ) and the arrival time t. The sky localisation is uniformly distributed across the celestial sphere, and the arrival time uniformly throughout the span of 1 yr. The polarisation follows a uniform distribution between 0 and 2π, while the inclination is sampled from $p(\iota) = \frac{1}{2}\sin(\iota)$ on the domain $[0, \pi]$. We will assume spinless black holes in this work, as the distributions for spin parameters are not observationally well constrained. This concludes the sampling of all the orientation angles (Fig. 4). The final binary black hole parameters to be sampled are the source frame masses and the redshift.

4.1.1 Sampling the mass distribution

From Sec. 2.3, we know that the source frame masses m_1 and m_2 fully determine the frequency evolution of spinless binary black hole mergers, and strongly influence their gravitational wave amplitudes. Heavier binaries curve spacetime more, and are hence detectable out to larger redshifts. The binary black hole mass distribution will thus heavily influence the observed lensed event rate, as well as the observed lensed binary black hole population.

Sampling the source frame masses is not a trivial exercise. An inference of the true mass distribution is done in Ref. [61] with the events from the second Gravitational Wave Transient Catalogue (GWTC-2). They investigated four different mass models, but we will only use the Power-law + Peak model in this work (Fig. 9), as it is the model that is most favoured by the data.

The model includes a rapidly falling power-law and a Gaussian "peak" at high masses, for the primary mass component. It is motivated by the possibility of a pile-up before the pair-instability gap, due to the mass loss in pulsational pair-instability supernovae. The pair-instability gap is the predicted absence of black holes with masses $\gtrsim 60$ M$_\odot$ produced by stellar collapse. Extremely heavy (> 130 M$_\odot$) dying stars produce highly energetic gamma rays, which can convert to electron-positron pairs in the presence of atomic nuclei. This conversion leads to a rapid drop in radiative pressure, which collapses the star and causes a runaway thermonuclear fusion explosion, leaving no remnant behind.

Pulsational pair-instability supernovae occur for slightly lighter stars ($100 - 130$ M$_\odot$), where the pair-instability is not sufficient to cause runaway explosions, but instead increases thermonuclear activity that return the star to equilibrium. After a few of these pulses, the star drops below 100 M$_\odot$, and can leave behind a black hole after the supernova. This causes a relative over-abundance of black holes just before the pair-instability gap. Note that formation channels other than stellar collapse can allow for higher-mass black holes.

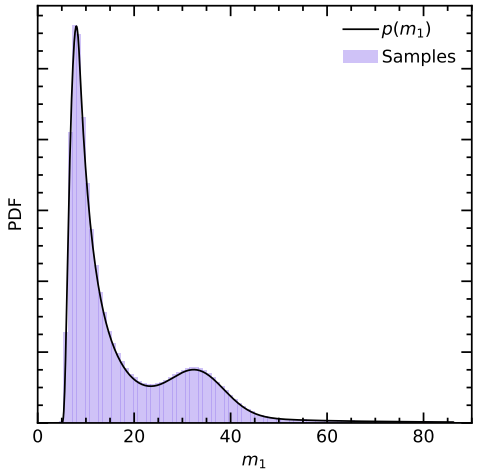

Parameter	Value
$\lambda_{\rm peak}$	0.10
α	2.63
β	1.26
μ_m	33.07 $M_\odot$
σ_m	5.69 $M_\odot$
$m_{\rm max}$	86.22 $M_\odot$
$m_{\rm min}$	4.59 $M_\odot$
δ_m	4.82 $M_\odot$

Table 1: All the values of the model parameters for the binary black hole mass distributions.

Figure 9: The probability distribution for the masses m_1, following the Power-law + Peak model from the GWTC-2 results. This is the mass model that is currently favoured by the available gravitational wave data.

The probability distribution is broken down according to $p(m_1, q|\theta_{\rm pop}) = p(q|m_1, \theta_{\rm pop})p(m_1|\theta_{\rm pop})$, with q the mass ratio m_2/m_1 and $\theta_{\rm pop}$ the underlying population parameters. The distribution for m_1 is given by

$$p(m_1|\lambda_{\rm peak}, \alpha, m_{\rm max}, m_{\rm min}, \delta_m, \mu_m, \sigma_m) = [(1 - \lambda_{\rm peak})\mathcal{P}(m_1| - \alpha, m_{\rm max}) + \lambda_{\rm peak} G(m_1|\mu_m, \sigma_m)]\, S(m_1|m_{\rm min}, \delta_m)\,, \tag{4.2}$$

with $\mathcal{P}$ a normalised power-law distribution with low and high mass cut-offs $m_{\rm min}$ and $m_{\rm max}$ and spectral index $-\alpha$. G is a Gaussian distribution with mean μ_m and width σ_m, and the parameter $\lambda_{\rm peak}$ gives the

fraction of binaries that follow the Gaussian. Finally, S is a smoothing function, which is defined as

$$S(m|m_{\min},\delta_m) = \begin{cases} 0 & m < m_{\min} \\ [f(m-m_{\min},\delta_m)+1]^{-1} & m_{\min} \leq m < m_{\min}+\delta_m \\ 1 & m \geq m_{\min}+\delta_m \end{cases}$$

$$f(m',\delta_m) = \exp\left(\frac{\delta_m}{m'} + \frac{\delta_m}{m'-\delta_m}\right).$$

The distribution for the mass ratio is defined for $q \leq 1$ and is given by

$$p(q|\beta, m_1, m_{\min}, \delta_m) \propto q^{\beta} S(qm_1|m_{\min},\delta_m)\,, \tag{4.3}$$

with β the spectral index of the power-law. Because of the complex nature of this combined distribution, we will break down the sampling step-by-step.

We can disect Eq. (4.2) as follows: the total population consists two sub-populations, that follow their respective distributions $\mathcal{P}$ and G. Before sampling these, we first draw a random number between 0 and 1 to determine which fraction of the total population gets sampled. If it is smaller than λ_{peak}, then G gets sampled, and vice-versa. This will give us values for m_1, but the total distribution still needs to be tailored by the smoothing function S at the low-mass end of the spectrum. We fix this by drawing random numbers u between 0 and 1, and rejecting samples where $u > S(m_1, m_{\min}, \delta_m)$. This will get rid of any excess low-mass samples. This whole procedure gives us a sample set that follows the correct probability distribution function (PDF), as we can see in Fig. 9. Sampling m_2 follows a very similar structure, with the simplification that there is only a single power-law as main distribution, which is then tailored by the smoothing function. This concludes the sampling of the masses of the binary components.

4.1.2 Sampling the binary black hole redshifts

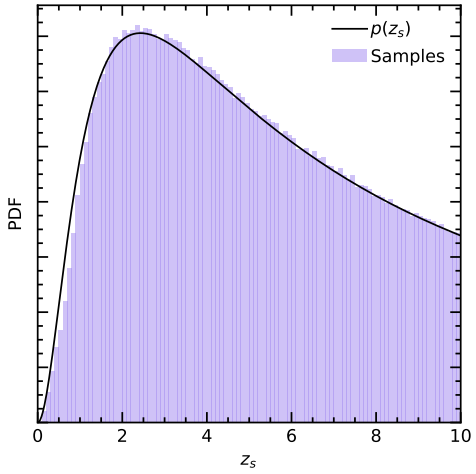

Parameter	Value
λ_z	0.563
a	2.906
b	0.0158
c	0.58
μ_z	1.1375
σ_z	0.8665

Table 2: All the values of the fitted parameters to $\mathrm{d}V_c/\mathrm{d}z_s$.

Figure 10: The targeted (black) and the sampled (purple) distributions for the source redshift z_s, which show the agreement between the semi-analytical approximation and the differential comoving volume.

The last binary black hole parameter we need to sample is the source redshift. We assume the binaries follow the differential comoving volume $\mathrm{d}V_c/\mathrm{d}z_s$, which can be normalised to give us $p(z_s)$. This normalisation is done on the domain $z_s \in [0, 10]$ (Fig. 10), as we do not expect to observe binaries at $z > 10$. We will use a semi-analytical approximation to $p(z_s)$ to accommodate for inverse transform sampling. This approximation

is given by $p(z_s) \simeq \lambda_z f(z_s|a,b,c) + (1-\lambda_z) g(z_s|\mu_z,\sigma_z)$, where f is a beta prime distribution centred at c

$$f(z) \propto (x-c)^{a-1}(1+x-c)^{-a-b}\,, \text{ and} \tag{4.4}$$

$$g(z) \propto \exp\left(-\frac{(\log(z)-\mu_z)^2}{2\sigma_z^2}\right)\,. \tag{4.5}$$

This approximation resembles the situation with the m_1 sampling (Eq. (4.2)), with the absence of a smoothing function. We can thus draw a number between 0 and 1 to choose a distribution based on λ_z, and sample the two distributions individually. Note that these both have to be normalised on the same domain as $\mathrm{d}V_c/\mathrm{d}z_s$, as their formal domains are $z_s \in [0,\infty]$.

With this, we can now sample all necessary binary black hole parameters. This procedure is repeated one million times, giving us a catalogue of binary black hole mergers.

4.2 The galaxy lens population

As we explained in Sec. 3.2, we will be using the Power-law Elliptical Mass Distribution (PEMD) galaxy lens model. The parameters that define a PEMD galaxy lens are: velocity dispersion σ_v, axis ratio q and spectral index of the density profile γ. We add to this an external shear, defined by γ_1 and γ_2, rotate the galaxy by ϕ_q and place the galaxy at redshift z_L. The shears encompass the effects of the galaxy's surroundings, and are drawn independently from a normal distribution centred at 0 and with a width of 0.05 [62, 63], while the axis rotation ϕ_q is random and follows a uniform distribution between 0 and 2π.

The remaining parameters follow distributions from the Sloan Digital Sky Survey (SDSS) catalogue, which is a large-scale redshift survey dedicated to spectroscopic and (previously) photometric observations of astrophysical sources throughout the Universe. This data has been combined with optical observations from the Hubble Space Telescope for the Sloan Lens ACS (SLACS) survey, which identified and studied strong gravitational galaxy-galaxy lenses. We take the density profile γ from the SLACS survey results [64], which follows a normal distribution with a width of 0.2, centred at 2. The distributions of the lens redshift z_L, velocity dispersion σ_v and axis ratio q are conditioned on the source redshift z_s, so a source is picked from the previously compiled binary black hole catalogue.

The lens redshift is then sampled in multiple steps. First, a value x between 0 and 1 is drawn from the distribution

$$p(x) = 30x^2(1-x)^2\,, \tag{4.6}$$

which gives the ratio between the comoving distance to the lens and the comoving distance to the source (see Appendix A.2 for the derivation). Given a source at redshift z_s, this ratio can then be translated to the redshift of the lens z_L. For the velocity dispersion, we choose the fit to elliptical galaxies only [63, 65]. We sample a parameter a from a generalised gamma distribution

$$p(a) = a^{\alpha-1}\exp\left(-a^\beta\right)\frac{\beta}{\Gamma(\alpha/\beta)}\,, \tag{4.7}$$

where $\alpha = 2.32$ and $\beta = 2.67$, and we take $\sigma_v = 161\mathrm{kms}^{-1} \times a$. We use the individual lensing probability to condition our distributions on strong lensing, as is required by the presence of $p(\theta_L, z_L|\mathrm{SL}, z_s)$ in the lensed rate integral (Eq. (3.18)). We approximate the Einstein radius θ_E as the Einstein radius of a singular isothermal sphere (SIS) lens (Eq. (3.15)) and take the individual strong lensing probability to be equal to the ratio between the sky area of the lens and the total sky area: $p(SL|\theta_L, z_L, z_s) = \pi\theta_E^2/4\pi \propto \theta_E^2$. All lenses are subsequently rejection sampled to condition them on the individual lensing probability, where we draw a uniformly distributed number between 0 and 3^2 and pass those that have a value $< \theta_E^2$.

Finally, we draw the axis ratio q from a Rayleigh distribution with scale $s = 0.38 - 0.09177a$[5]

$$p(q) = \frac{1-q}{s^2}\exp\left(-\frac{(1-q)^2}{2s^2}\right)\,, \tag{4.8}$$

[5] Ref. [63] has a typo, we use the correct scaling from the LensPop code.

which is sampled until we get a value $0.2 < q < 1$ to exclude highly flattened profiles. This concludes the sampling of the galaxy lens parameters. We need to draw a source position in the lens plane $\vec{\beta}$ as well, in order to solve the lens equation. Since we are only interested in strong lensing configurations, we draw uniformly distributed positions around/inside the lens area until we get a solution with 2 or more images. This effectively incorporates $p(\vec{\beta}|SL)$ from Eq. (3.18).

Once a lens and a source position is drawn, the lens equation is solved using the LENSTRONOMY package, which is a multi-purpose package for modelling strong gravitational lensing [66, 67]. Its lens equation solver gives us the images of the lensed configuration, each with a magnification, time-delay and image type. We repeat this whole process for a million randomly chosen sources from the binary black hole catalogue, and save the results in a new catalogue, our final lensed event catalogue.

4.3 Analysing the data

Only detectable events are to be included in our analysis, and we choose the optimal signal-to-noise ratio (SNR) ρ as our detection criterium (see Eq. (2.29) with $s = h$), as it quantifies the strength of a signal within our detectors. We calculate the SNR of the lensed waveform, and both the time-delay factor and Morse phase drop out because of the complex conjugate. This leaves only the frequency-independent magnification, which can be taken out of the integral. Another frequency-independent factor is the antenna pattern (Eq. (2.27)), and finally the SNR is inversely related to the luminosity distance. This gives us the SNR at the detector [68]

$$\rho_{j,\mathrm{det}} = |\mu_j|^{1/2} A(\iota, \psi, \alpha, \delta, t_{\mathrm{arrival}}) \rho_{1\mathrm{Mpc}}(m_1^z, m_2^z) \frac{1\mathrm{Mpc}}{D_S}\,, \tag{4.9}$$

where $\rho_{1\mathrm{Mpc}}$ is the SNR of an optimally oriented source with redshifted masses $m_{1,2}^z = (1+z)m_{1,2}$ at a luminosity distance of 1 Mpc

$$\rho_{1\mathrm{Mpc}} = \int_{f_0}^{f_{ISCO}} \mathrm{d}f\, \frac{\tilde{h}^*(f)\tilde{h}(f)}{S_n(f)}\,, \tag{4.10}$$

for a single detector, with f_0 the lowest frequency said detector can measure and $\tilde{h}(f)$ the waveform associated with the redshifted masses, for which we will use the IMRPHENOMD model [55, 69]. Eq. (4.9) can easily be extended to a multiple detector network by adding the SNRs in quadrature. Under the assumption that all detectors have a similar power spectral density (PSD) $S_n(f)$, this equates to adding the antenna pattern functions in quadrature, e.g. for a network consisting of three detectors $A_{\mathrm{network}} = \sqrt{A_1^2 + A_2^2 + A_3^2}$. We assume a four-detector network consisting of LIGO-Livingston and Hanford, Virgo, and KAGRA, and use analytical versions of the PSDs from LALSimulation, which is a package providing waveform and noise generation routines [70].

All events with a network SNR > 8 are counted as detectable, and are counted in the sum with a weight $\tau(z_s)\mathcal{R}(z_s)/(1+z_s)$ ($= f(x)$ from Eq. (4.1)). This weight quantifies an event's *true* occurrence, and will be used to quantify the importance of all the events. We use the semi-analytical approximation to the merger-rate density from [35], and re-scale it to fit the observed local merger-rate $\mathcal{R}_0 = 23.9^{+14.3}_{-8.6}$ Gpc^{-3} yr^{-1}

$$\mathcal{R}(z_s) = \frac{\mathcal{R}_0(a_4+1)e^{a_2 z_s}}{a_4 + e^{a_3 z_s}}\,, \tag{4.11}$$

with the fitted parameters $a_2 = 1.6$, $a_3 = 2.1$ and $a_4 = 30$. The semi-analytical approximation is derived through a fit to the results of population-synthesis codes. We assume distributions from the SDSS catalogue for early-type galaxies, and follow Ref. [40] in their derivation for the strong lensing optical depth, which we detail in Appendix A.2. The optical depth is then given by

$$\tau(z_s) = 4.17 \times 10^{-6} \left(\frac{r(z_s)}{1\ \mathrm{Gpc}}\right)^3\,, \tag{4.12}$$

where $r(z_s)$ is the comoving distance to the source. The optical depth and merger-rate density, combined with the detection threshold on the SNR, are all the tools we need for analysing the data from the catalogue.

5 The population

The population consists of one million binary black holes (Sec. 4.1), which have been forcibly strongly lensed by galaxy lenses (Sec. 4.2), each producing two or more images. This gives us a final dataset of roughly 2.2 million images, each labeled by the source and lens parameters (which are the same for images from one event), and their magnification, time-delay and image type (which are unique). The following section will demonstrate the versatility of this dataset through performing a set of separate analyses on the data. These analyses are not intended to be exhaustive, and we refer the interested reader to the full dataset with some sample analysis code [71]. All uncertainties quoted in this work are at the 90 % confidence level, and we assume a flat ΛCDM cosmology with $H_0 = 70\,\mathrm{km\,s^{-1}\,Mpc^{-1}}$ and $\Omega_m = 0.31$.

5.1 Event rates

We start by calculating the observed lensed event rate (Eq. (3.18)), with the added condition that at least two images need to be detectable. This requirement is based on the fact that at least two images are needed for lensed event identification during searches, since there is a degeneracy between the magnification and luminosity distance (Eq. (3.11)). We also scale the results from images to events, such that a lensed event consisting of two super-threshold images is only counted once in the integral. We find that the total observed rate of lensed events is $1.3^{+0.6}_{-0.4}\ \mathrm{yr^{-1}}$. The observed rate of unlensed events is $\sim 1900\ \mathrm{yr^{-1}}$ (Eq. (2.33)), which gives us a relative rate of about 1 lensed event for every 1500 unlensed events.

We can extend these forecasts to the future LIGO A+ detector upgrade, as well as the planned Voyager detector that might replace A+ eventually. We show these rates in Table 3, including sub-categories for the different number of *observed* super-threshold images. Note that the number of observed images is not directly correlated with the original number of images produced by the lensed configuration, i.e. there can be demagnified images below the detection threshold which are not counted.

Observed rates		L	L/H/V/K	L/H/V/K (A+)	L/H/V/K (Voyager)
Lensed events:	total	$0.21^{+0.10}_{-0.07}\ \mathrm{yr^{-1}}$	$1.3^{+0.6}_{-0.4}\ \mathrm{yr^{-1}}$	$3.3^{+1.7}_{-1.1}\ \mathrm{yr^{-1}}$	$16.8^{+8.4}_{-5.6}\ \mathrm{yr^{-1}}$
	double	$0.17^{+0.08}_{-0.06}\ \mathrm{yr^{-1}}$	$0.92^{+0.46}_{-0.31}\ \mathrm{yr^{-1}}$	$2.5^{+1.2}_{-0.8}\ \mathrm{yr^{-1}}$	$13.1^{+6.5}_{-4.4}\ \mathrm{yr^{-1}}$
	triple	$0.032^{+0.016}_{-0.011}\ \mathrm{yr^{-1}}$	$0.23^{+0.12}_{-0.08}\ \mathrm{yr^{-1}}$	$0.55^{+0.28}_{-0.19}\ \mathrm{yr^{-1}}$	$2.0^{+1.0}_{-0.7}\ \mathrm{yr^{-1}}$
	quadruple	$0.011^{+0.005}_{-0.004}\ \mathrm{yr^{-1}}$	$0.12^{+0.06}_{-0.04}\ \mathrm{yr^{-1}}$	$0.30^{+0.15}_{-0.10}\ \mathrm{yr^{-1}}$	$1.6^{+0.8}_{-0.6}\ \mathrm{yr^{-1}}$
Unlensed events		$370\ \mathrm{yr^{-1}}$	$1.9 \times 10^3\ \mathrm{yr^{-1}}$	$5.8 \times 10^3\ \mathrm{yr^{-1}}$	$31 \times 10^3\ \mathrm{yr^{-1}}$
Relative occurrence		1 : 1760	1 : 1500	1 : 1740	1 : 1830

Table 3: The observed event rates for different LIGO sensitivities, categorised according to the observed number of super-threshold images. We report the rates for solely the Livingston detector (L), as well as the rates with the inclusion of the Hanford (H), Virgo (V) and KAGRA (K) detectors. Keeping the sensitivities of Virgo and KAGRA fixed, we make projections for the future A+ and Voyager upgrades of the two LIGO detectors. Furthermore, we report the relative rates of lensed and unlensed event detections, as those are less sensitive to uncertainties in the merger-rate density.

Detector upgrades will significantly increase the number of lensed event detections, but there are methods for finding images that allow us to enhance the observed rates in the present day and age. When at least one super-threshold sibling image is available, targeted lensed searches may allow us to uncover so-called sub-threshold triggers below the usual noise threshold [72, 73]. The strain data is searched with a reduced template bank centred around the super-threshold trigger, effectively lowering the background SNR from noise and glitches. We classify a sub-threshold event as an event trigger observed below an SNR of 8, but above an SNR of ρ_{th}. Sub-threshold events can be considered detectable when they have at least one super-threshold sibling image. Since $\rho \propto d_L^{-1}$, Ref. [72] provides us with an indicative increase in the effective distance of $\sim 15\%$, corresponding to $\rho_{th} = 7$, which we take to be illustrative for a sub-threshold search.

Observed rates	L	L/H/V/K	L/H/V/K (A+)	L/H/V/K (Voyager)
Lensed events: total	$0.30^{+0.15}_{-0.10}$ yr^{-1}	$1.7^{+0.9}_{-0.6}$ yr^{-1}	$4.3^{+2.1}_{-1.5}$ yr^{-1}	$19.9^{+9.9}_{-6.7}$ yr^{-1}
double	$0.23^{+0.12}_{-0.08}$ yr^{-1}	$1.2^{+0.6}_{-0.4}$ yr^{-1}	$3.2^{+1.6}_{-1.1}$ yr^{-1}	$15.6^{+7.8}_{-5.2}$ yr^{-1}
triple	$0.054^{+0.027}_{-0.018}$ yr^{-1}	$0.32^{+0.16}_{-0.11}$ yr^{-1}	$0.71^{+0.35}_{-0.24}$ yr^{-1}	$2.3^{+1.1}_{-0.8}$ yr^{-1}
quadruple	$0.015^{+0.008}_{-0.005}$ yr^{-1}	$0.18^{+0.09}_{-0.06}$ yr^{-1}	$0.43^{+0.21}_{-0.14}$ yr^{-1}	$2.0^{+1.0}_{-0.7}$ yr^{-1}
Relative occurrence	1 : 1210	1 : 1100	1 : 1350	1 : 1540
Overall increase	45 %	36 %	29 %	19%

Table 4: The observed event rates for different LIGO sensitivities including sub-threshold triggers with an SNR > 7, categorised according to the observed number of super- and sub-threshold images. Virgo and KAGRA are always assumed to be at design sensitivity, when included in the detector network. We take SNR > 7 as a proxy for the detection capabilities of the sub-threshold searches, but the actual improvements achieved may vary.

We find that the total number of observed quadruply lensed events increases from $0.12^{+0.06}_{-0.04}$ yr^{-1} to $0.18^{+0.09}_{-0.06}$ yr^{-1}, an increase of 51%, when including sub-threshold triggers. Furthermore, the total number of observed triply lensed events increases with 40% from $0.23^{+0.12}_{-0.08}$ yr^{-1} to $0.32^{+0.16}_{-0.11}$ yr^{-1} and for doubly lensed events there is an increase of 33% from $0.92^{+0.46}_{-0.31}$ yr^{-1} to $1.2^{+0.6}_{-0.4}$ yr^{-1}. We extend these calculations to the different sensitivities and detector networks presented earlier, and report the observed number of events in Table 4, categorised according to the detected number of super-threshold and sub-threshold events. The increase in detectable events demonstrates how crucial performing follow-up sub-threshold searches for the lensed counterpart pairs of super-threshold events, giving further impetus to such searches.

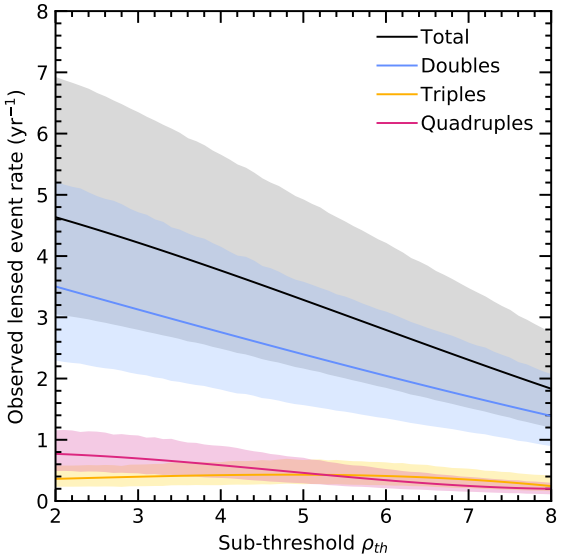

$P(\rho) = a_0 + a_1\rho + a_2\rho^2 + a_3\rho^3$

	Number of images		
	2	3	4
a_0	4.26	3.03×10^{-1}	7.32×10^{-1}
a_1	-3.78×10^{-1}	1.64×10^{-2}	1.02×10^{-1}
a_2	-1.44×10^{-3}	9.78×10^{-3}	-4.85×10^{-2}
a_3	4.78×10^{-4}	-1.59×10^{-3}	3.42×10^{-3}

Table 5: A third-order-polynomial fit to the mean detection rates from Fig. 11, as a function of sub-threshold detection threshold SNR.

Figure 11: The observed detection rates as a function of sub-threshold detection threshold SNR ρ_{th} for double (blue), triple (yellow) and quadruple (magenta) lensed event detections and the total rate (black). The shaded areas indicate the uncertainty from the local merger rate. The observed rates increase several multiples as the threshold SNR decreases, most notably the quadruple rates. Sub-threshold searches can thus greatly increase the probability of detecting lensed events.

However, because the sub-threshold searches vary in their sensitivity and some further improvements are still pending, the SNR threshold choice may vary. During actual searches, different detectability criteria from the

SNR are used, and the SNR can be considered a proxy that correlates with these criteria, but not perfectly. Thus, we also give a phenomenological fit to the SNR distribution, which can extrapolate our results to any choice of SNR threshold. In particular, we demonstrate a third-order-polynomial fit to the detection rate as a function of the SNR threshold for double, triple, and quadruple images (see Fig. 11 and Table 5).

There are several caveats associated with all of these predicted observed event rates. Detector down-time is not included in the absolute rates, which is the reason we report the relative rates as well. The number of detected unlensed events during an observing run can then be scaled, using the relative rate, to find the predicted number of lensed events. Secondly, we assumed an optical depth derived for SIS lenses (Appendix A.2). A study was performed using elliptical SIE lenses [36], but only a difference of 4% was found, which is significantly smaller than the error on the local merger rate. We have thus ignored corrections from the ellipticity of the lenses.

Finally, the merger-rate density is largely unconstrained at high redshifts, which is where our lensed sources are located. While this introduces an extra uncertainty to our projected rates, Ref. [48] shows how the non-detection of lensed events can help constrain the merger-rate density at high redshifts. Conversely, regular detections of lensed events can help constrain the delay between the star formation rate and the merger rate at high redshifts, allowing us to probe the formation channels of binary black holes [74]. Consequently, while our forecasts are *tentative* based on our best understanding of the binary black hole and lens population, the comparison between our theoretical predictions and future observations will increase our understanding of binary black holes themselves.

5.2 Time-delays and image types

One final caveat is that our rates do not take into account the intricacies of finding a lensed event from within a wealth of data. We will show how our predictions for the lensing signatures can help improve the accuracy of the searches, but first we need to investigate these signatures and quantify their properties.

From Sec. 3.1, we know of three major effects of lensing on the waveform: a magnification, time-delays between the images, and the image type quantified by the Morse phase. The magnification is degenerate with the luminosity distance, and is thus hard to determine precisely in an analysis. The image type and

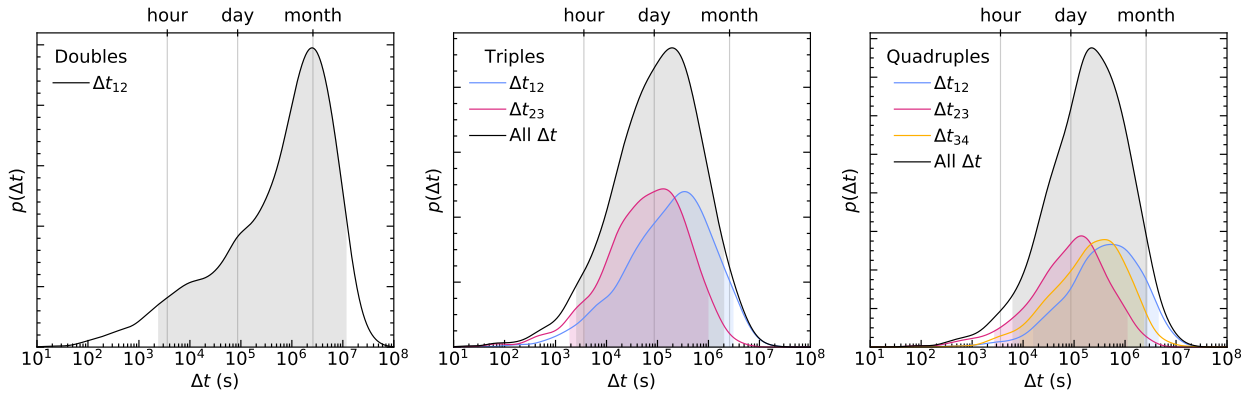

Figure 12: **(a)** The time-delay distribution for double images. The shaded regions give the 90 % confidence intervals for $\Delta t_{12} \sim 0.7$ hr $-$ 133 days. **(b)** The time-delay distributions (with confidence intervals) for triply lensed sources between the first two images (blue), between the second and third images (magenta) and the sum of those two (black). **(c)** The time-delay distributions (with confidence intervals) for quadruply lensed sources between the first two images (blue; $\sim$ 4.5 hr $-$ 51 days), the second and the third images (magenta; $\sim$ 0.8 hr $-$ 13 days), the last two images (yellow; $\sim$ 2.4 hr $-$ 27 days), and the total of the three (black; $\sim$ 1.8 hr $-$ 31 days). Generally, the time delay between the lensed pairs is $\lesssim 90$ days.

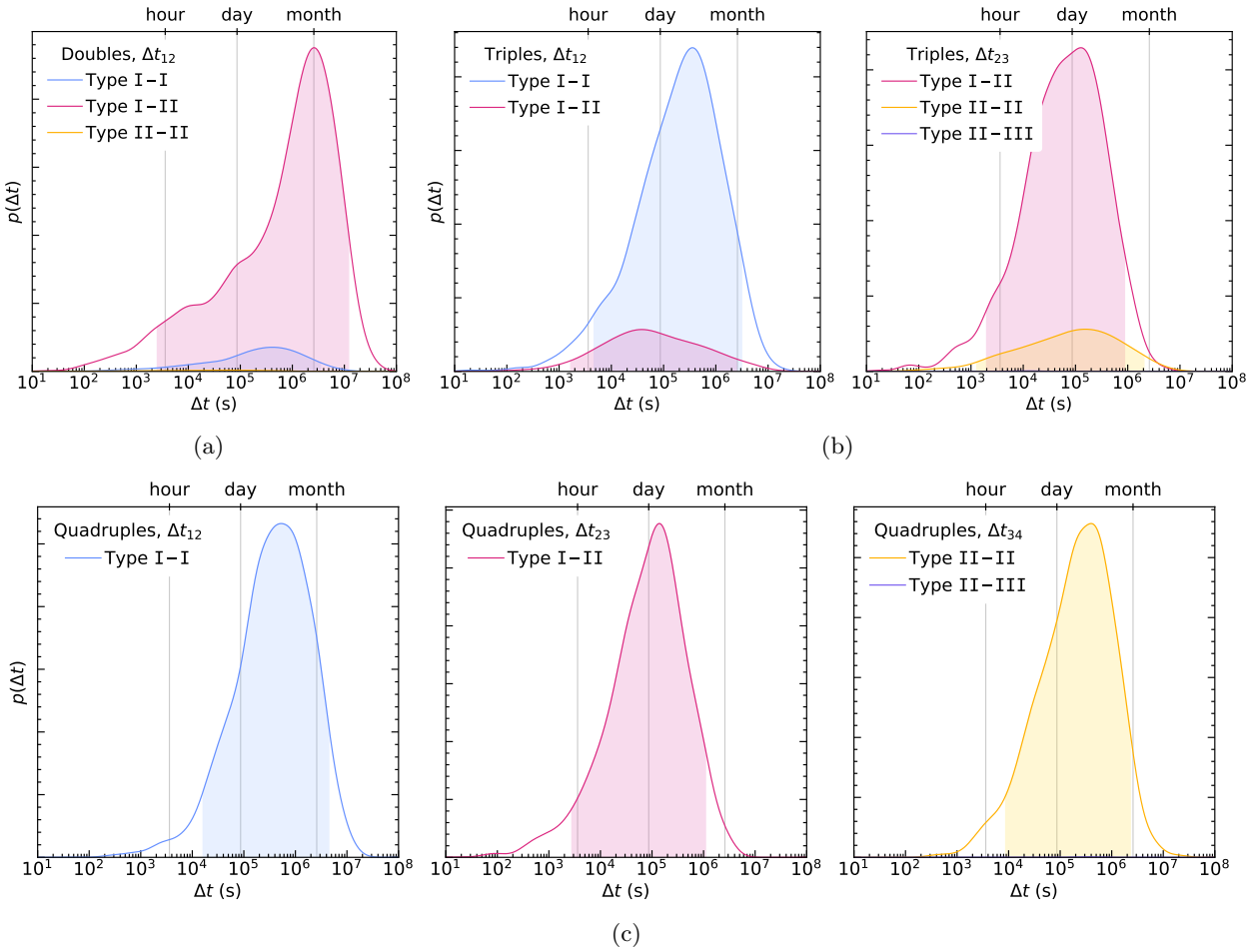

Figure 13: The time-delay distributions for *observed* doubly, triply and quadruply lensed events, separated by image type and scaled to show relative occurrence within a plot. The legend entries mark the image types of the two associated images, and combinations not present within the data are not shown in the legend. Type I-II images from doubly lensed events have significantly higher time delays than quadruples, illustrating the discriminatory power of the combined measurement of image types and time delays.

time-delay are closely linked though, as the image type is a derived property of the time-delay function. We show the time-delays between images for observed doubly, triply and quadruply lensed systems in Fig. 12. The most striking feature in Fig. 12 is that observed triply and quadruply lensed events typically have time-delays of less than a month, while doubly lensed events can go up to $4-5$ months. The tail at small time-delays in Fig. 12a is also an indication that some of the original systems have more than two images.

We further break down the time-delays according to their image types in Fig. 13, where "Doubles, Δt_{12} −Type I-I" signifies two consecutive images, both Type I, that are observed as a doubly lensed event, and similarly for the remaining entries. There is a clear correlation between the chronological order of the images and the image types. Generally, the Type Is come first, followed by the Type IIs, and once in a blue moon a Type III is detectable. From the discussion on image types, we know that two consecutive Type IIs can only occur within a quadruply or quintuply lensed system, while two consecutive Type Is require the existence of at least three images total. Ascertaining the image types of lensed candidates can thus provide valuable information on the original system, and help motivate follow-up sub-threshold searches.

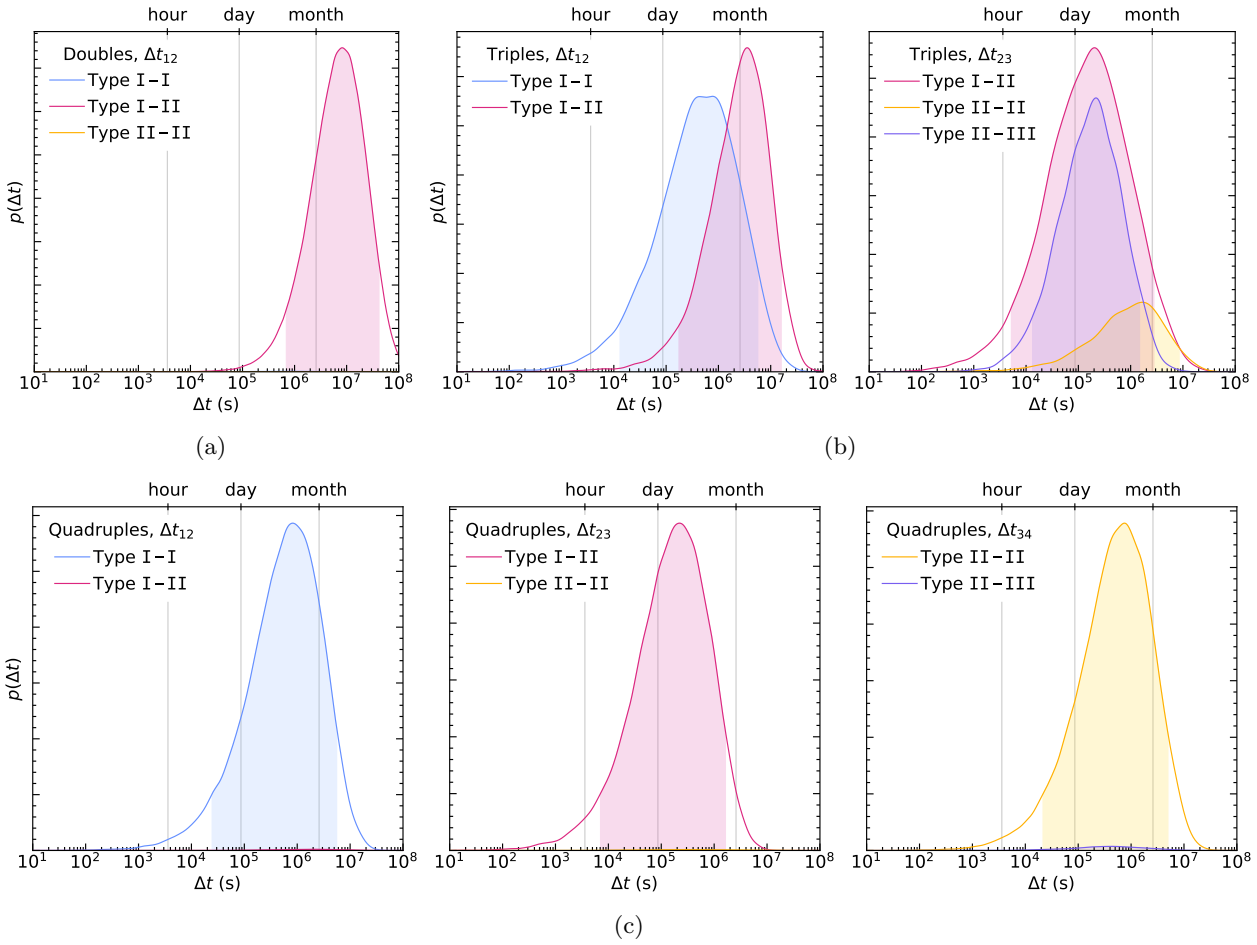

Figure 14: The time-delay distributions for *all* doubly, triply and quadruply lensed events, separated by image type and scaled to show relative occurrence within a plot. These show distinctly different signatures between the multiplicities of the lensed systems, representing their fundamental configurational differences (see Sec. 3.1).

While Fig. 13 is already quite insightful on in its own right, it can be best interpreted when compared to the total population, which is compiled without the detectability requirement (Fig. 14). Truly doubly lensed events have the largest time-delays, ranging from a week to several months at 90 % confidence, while the second (Type I) and third (Type II) image of a quadruple follow within a month of each other. Only 0.3 % of doubles have time-delays of less than a day, so such a detection would likely come from an originally quadruply lensed event. Fig. 14b clearly shows the two different arrangements that can cause triple lensing: either Type I-I-II or Type I-II-III images in chronological order. A small but significant fraction has ordering I-II-II, which points towards a limitation of LENSTRONOMY. These events are likely quadruply lensed, but the angular separation between the first two type Is is too small for LENSTRONOMY to resolve. However, triply lensed systems are significantly less common than quadruply lensed systems within the total population, so we do not expect this issue to affect our predicted event rates from Sec. 5.1.

Galaxy clusters can cause strong lensing as well, and predictions of their rates have been made as well [75]. However, their expected time-delays are typically larger than a year, extending past the regular observation-run time. This significantly decreases the probability of two or more images from galaxy cluster lensing to occur within a single observation run, making their detection unlikely. We thus advise future and ongoing searches to focus on galaxy lensing, as its properties are more convenient and constrained through the lensing statistics presented in this section.

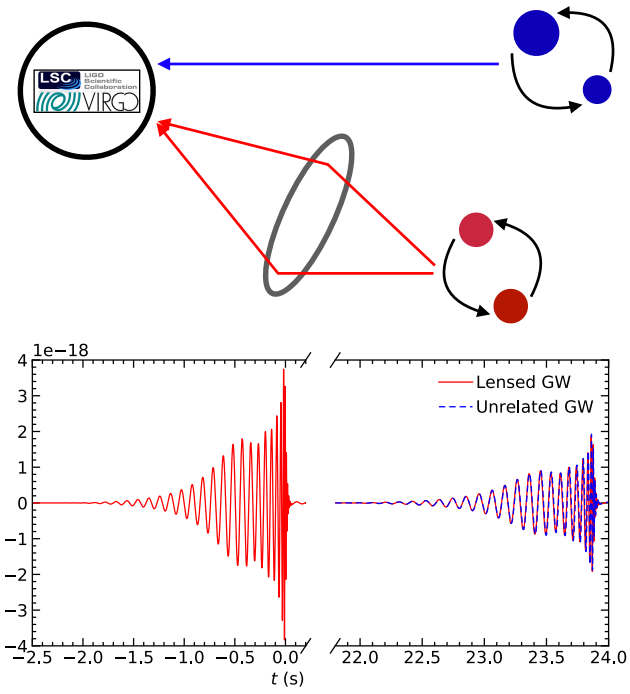

Figure 15: A set of different BBH signals. Red is a $m_1 = m_2 = 100M_\odot$ BBH at a luminosity distance of 1 Mpc, which is subsequently lensed by an singular isothermal sphere (SIS) lens of $10^6 M_\odot$. Blue is a $m_1 = 120M_\odot$ and $m_2 = 84M_\odot$ at 1.2 Mpc. The degeneracy between the magnification and distance is clearly visible. The second signal mimics a lensed signal, which would give rise to a false alarm.

5.3 The false alarm probability

With these detailed predicted distributions on our side, we can tackle the endeavour that is actually finding a lensed event from dozens, if not hundreds or thousands detections during an observing run. There are currently two steps in identifying a lensed event. The first is to find a counter-image of a super-threshold event with a matching waveform [72, 73]. The second is to test if the two waveforms are identical within detector accuracy (save for an overall difference in the complex phase, arrival time, and amplitude), as expected of the lensing hypothesis [40, 45–47]. However, it is also possible for two waveforms to be near-identical within detector accuracy by chance, giving rise to a false alarm probability (see Fig. 15, for an illustration).

We now know the expected distributions of the time-delays (Fig. 12), as well as the distribution for uncorrelated events [43]. This allows us to calculate a ranking statistic

$$\mathcal{R}_U^L = \frac{p(\Delta t|\text{Lensed})}{p(\Delta t|\text{Unlensed})}\,, \tag{5.1}$$

which quantifies how much more likely a certain time-delay is under the lensed hypothesis than under the unlensed one. The distribution of $\mathcal{R}_U^L$ values differs between lensed and unlensed events, as can be seen in Fig. 16a. The survival function for unlensed events is of particular interest, since it tells us the fraction of unlensed events that have a similar or higher $\mathcal{R}_U^L$ than an event with a given $\mathcal{R}_U^L$. As an example, we take $p(\Delta t|\text{Lensed})$ to be the average distribution for quadruply lensed events, calculate $\mathcal{R}_U^L$ for both lensed and unlensed events, and check the value of the survival function for a large sample of events from the lensed distribution. This gives us an average of 0.029 unlensed events producing an $\mathcal{R}_U^L$ similar or higher than a given lensed event, or equivalently, a reduction of the individual false alarm of a truly lensed event by a factor of 34. Incorporating knowledge from the expected time-delay distribution thus greatly improves the significance of lensed event candidates.

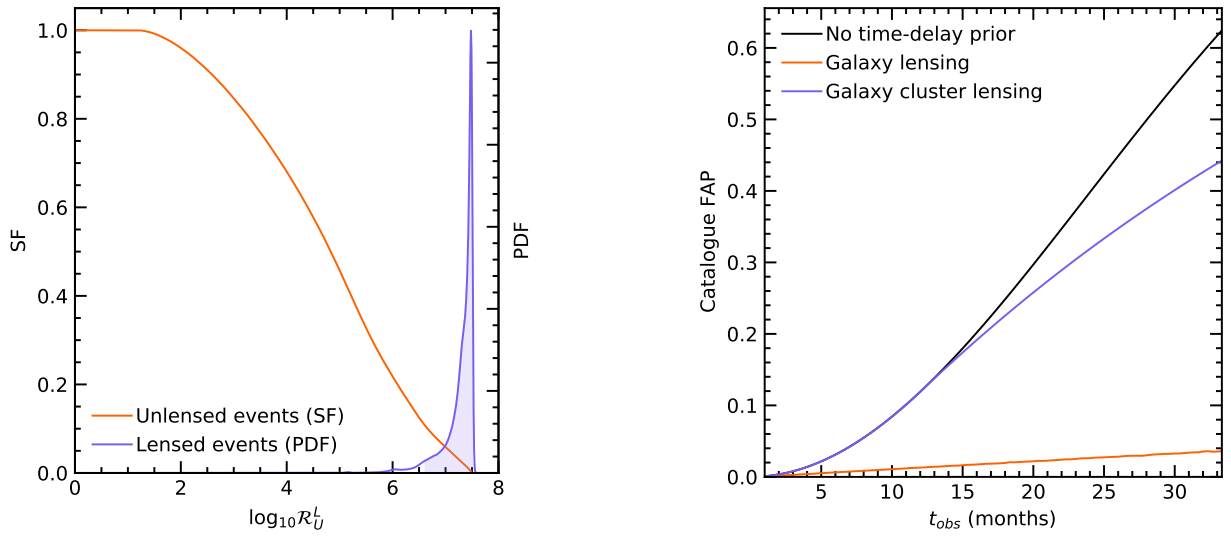

(a) (b)

Figure 16: **(a)** The $\mathcal{R}_U^L$ distributions assuming unlensed events (orange) and lensed events (purple). For unlensed events, the survival function (SF) is plotted, which is 1 − CDF (cumulative distribution function). Only a small fraction of unlensed events have an $\mathcal{R}_U^L$ similar or higher than lensed events, illustrating the $\mathcal{R}_U^L$'s ability to differentiate between lensed and unlensed events. **(b)** The catalogue false alarm probabilities (FAP) as a function of the observation run times t_{obs}, assuming a constant event rate $N = 510$ events/yr, time window $\Delta t_{\rm cluster} = 1$ yr and an intrinsic FAP $= 10^{-6}$. Shown are the FAP without windowing (black), the windowed FAP for galaxy cluster lensing (purple), and the ranked FAP for galaxy lensing (orange). Incorporating the galaxy-lensing time-delay changes the functional dependency in the exponential from $\propto t_{obs}^2$ to $\propto t_{obs}$. This reduces the FAP significantly for galaxy lensing when $t_{obs} \sim 1$ yr, but galaxy cluster lensing requires much longer observation times.

However, the improvement from incorporating the time-delay distribution becomes even more apparent when we consider a catalogue of detections. The total catalogue false alarm probability, that there is at least one false alarm within $N_{\rm pairs}$ of unlensed events, is given by

$$\mathrm{FAP} = 1 - \prod_{i=0}^{N_{\rm pairs}} (1 - p_i)\,, \tag{5.2}$$

where p_i is the individual false alarm. It consists of an intrinsic false alarm probability from the true binary black hole population, and the likelihood of the time delay between the unlensed events occurring under the lensed hypothesis.

Without time-delay information, all events N from the observing run need to be taken into account with equal weight, giving $N_{\rm pairs} = N(N-1)/2$, where N is the total number of single events. This quadratic dependence makes the occurrence of a false alarm increasingly probable for long observing runs and/or high unlensed event rates. As we showed in Sec. 5.1, the unlensed event rate is expected to be $\sim 10^3$ yr^{-1} as we reach LIGO design sensitivity, giving over half a million pairs for our lensed event analysis. Even if the intrinsic false alarm probability is low, the inevitability of a false alarm in the dataset will raise concerns over the significance of a possible lensed event candidate detection.

Assuming an intrinsic false alarm probability $p = 10^{-6}$ as an underestimation, we find that the complexity of the total catalogue false alarm probability becomes linear, similar to typical single-event false alarms, when including galaxy lensing statistics (Fig. 16b). The weights assigned to the event pairs are the values of the cumulative distribution for the $\mathcal{R}_U^L$s of lensed events, since this is the fraction of lensed events that have a similar

or lower significance than an unlensed event with a given $\mathcal{R}_U^L$. For galaxy cluster lensing, we assumed all events with time-delays of less than a year to be equally likely, and rejected all events with larger time-delays.

The catalogue false alarm probability grows with the number of detections N when taking galaxy time-delays into account, instead of with the number of pairs $N(N-1)/2$. Such a low total false alarm probability strengthens the significance of any possible detected lensed candidates. Furthermore, incorporating the knowledge of the predicted time-delay distributions would allow us to tackle the problem created by the otherwise rapidly rising false alarm.

A noteworthy feature of the time delay is the correlation between the time-delays of subsequent images from the same event. Fig. 17 shows the two-dimensional density functions of the time delays for observed quadruply lensed events, and a linear correlation between the ordered images can be made out. Such multi-dimensional probabilities can be used to perform lensed event analyses beyond trigger pairs, and thus further reduce the false alarm probability.

An important caveat is that the time-delay distributions are dependent on the lens modelling and the astrophysical priors, and no uncertainties were included in their calculation. Lensed event identification based on these specific distributions might introduce a model bias, which would harm our search capabilities. If incorporated during lensed event searches, the time-delay distributions as presented in this work should be relaxed to allow for variations in the true lens population, correcting for possible biases.

Another factor is the dependence of the individual false alarm probability on the binary black hole population. From the mass distribution (Fig. 9), one can observe immediately that binary black hole mergers with masses $\sim 50\ \mathrm{M}_\odot$ are less likely to occur than mergers with $\sim 10\ \mathrm{M}_\odot$. While the true mass distribution of the binary black hole population may vary from Fig. 9, the concept stays the same. More research is thus needed to identify the dependency of the individual false alarm probability on the binary black hole population.

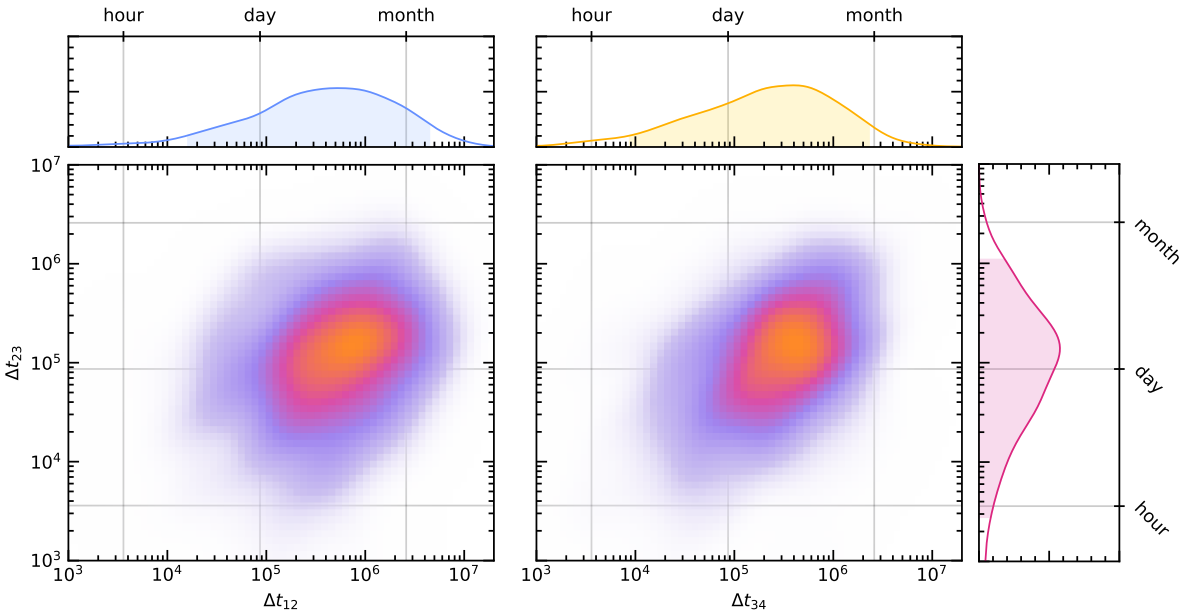

Figure 17: The two-dimensional density functions for consecutive images from observed quadruply lensed events. The matching one-dimensional distributions from Fig. 12 are shown to the sides. Both density functions show linear correlation, which can be employed to reduce the false alarm of quadruply lensed detection even further.

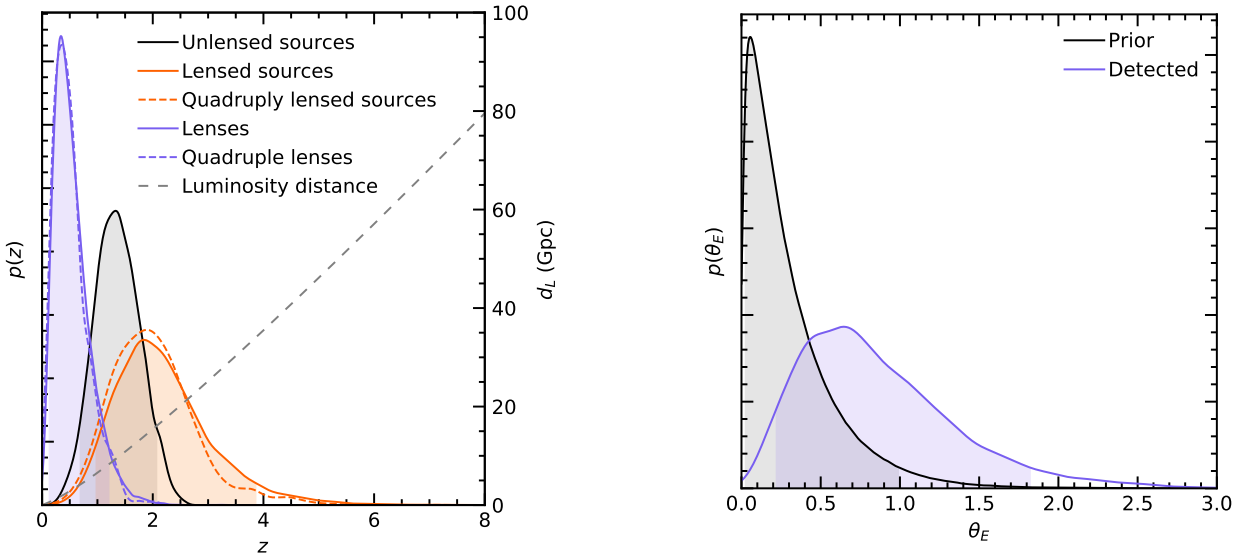

(a) (b)

Figure 18: **(a)** The observed redshift distributions for the galaxy lenses (purple) and lensed sources (orange). The unlensed observed source distribution (black) is shown for comparison. Additionally, we show the distributions specifically for events that have been quadruply lensed (dashed), as an example of the versatility of the data. The 90% confidence interval for the unlensed sources is $z_s \sim 0.7-2.1$, while for the lensed sources $z_s \sim 1.0-3.9$. Lensing magnifications and optical depth thus allow us to probe events beyond the regular detector horizon. **(b)** The observed (purple) and original (black) distributions for the Einstein radii. The Einstein radii of observed lensed systems are typically $\sim 0.2-1.8$ arcsec, while the prior population has Einstein radii $\theta_E < 1.0$ arcsec. The Einstein radius will play an important role in localisation efforts.

5.4 The observed source and lens populations

Once we have identified an event with a high likelihood of being lensed, its estimated source and lens parameters can be used in further analyses. When four images are observed, we essentially measure the events sky position $4-16$ times (depending on how many detectors are operational). This allows for constraints of < 10 deg^2 on the sky area containing the merger [23]. This area of the sky can then be searched with optical telescopes, identifying all possible lens + host galaxy combinations. Through modelling the time-delays and magnifications of the electromagnetically observed systems, the best match with the observed gravitational waves can be calculated. This provides us with a possible identification of the host galaxy. If realised in practice, such identification might allow for e.g. improved lens modelling and studies on binary black hole formation.

We present our expected observed redshift distributions for both lenses and sources in Fig. 18a. Observed lensed sources are predicted to lie within $z_s \sim 1.0-3.9$, beyond the current detector horizon of $z_s \sim 1$. Observability of lenses in the electromagnetic spectrum hinges on a set of requirements based on the telescope's specifications. While we cannot comment on the observability of the host galaxies, as we did not incorporate those in this work, we present the predicted observed distribution of the Einstein radii in Fig. 18b. As an estimate of observability, an Einstein radius of $\gtrsim 0.3$ arcsec is required for the Euclid telescope (Wempe et al., in prep.), which is satisfied by ~ 90 % of lenses in our sample.

This percentage is highly dependent on the choice of the velocity dispersion distribution. Distributions based on all-type galaxies (not just ellipticals) peak at lower velocity dispersions when conditioned on strong lensing [76]. While this is an important caveat to note, we do not expect our choice of the velocity dispersion distribution to influence our predicted rates, as the lenses are conditioned on strong lensing regardless.

If the host galaxy can be localised, precise redshift-luminosity distance measurements can be made by combining electromagnetic and gravitational wave observations. These can in turn be used to calibrate the cosmological model and measure the Hubble constant H_0. Another line of research is the measurement of gravitational wave polarisations beyond h_+ and $h_\times$. Alternate theories to GR allow up to six total polarisations, each having a different beam pattern function [77] (see Eq. (2.25) for the + and × responses). Since detectors only see the total response, precise sky localisations and the detection of multiple images provide the discriminatory power necessary for measuring the individual polarisations. These measurements provide a novel test of GR and alternate theories, likely improving our understanding of fundamental physics itself.

6 Conclusions

Gravitational waves can be lensed by massive galaxies, much like light. This phenomenon opens up possibilities for altogether new fields of research in cosmology. In this work, we have created a catalogue of one million strongly lensed binary black holes (BBHs), from observationally constrained distributions of the source and lens parameters. We predict $1-2$ lensed event detections per year at LIGO design sensitivity, in conjunction with the Virgo and KAGRA detectors. These rates will increase as LIGO receives further upgrades, and more detectors become available. One can also enhance the number of detections by performing rigorous sub-threshold searches, for which the methodologies are already developed and continuously being improved.

We then presented detailed predicted time delay distributions, and showed the link between the image type and time-delay. This information can prove useful for discerning whether the source was originally doubly, triply or quadruply lensed. These distributions can be used as well to improve ongoing and future lensed event searches, by assigning lensed event candidates a significance based on our lensing statistics. We demonstrate how the false alarm probability of a lensed event can be reduced by a factor ~ 30, while the catalogue false alarm probability changes complexity from a quadratically to a linearly increasing trend. This change significantly decreases the probability of a false alarm during upcoming observing runs, and underlines the importance of taking lensing statistics into account.

Finally, we showed our results for the expected observed distributions of source and lens redshifts, as well as Einstein radii. These quantities will play an important role in precise sky-localisation endeavours, which are a requirement for several science cases such as Hubble constant measurements. We cannot possibly present all interesting statistics in this work, so we encourage the interested reader to investigate the data themselves. Anyone in need of properties of lensed gravitational waves (or a subset thereof) can find their relevant distributions in our catalogue [71].

It is our hope that this work and its subsidiary publication [49] will help motivate increased effort into lensed event searches, as well as the incorporation of lensing statistics into those searches. Lensed gravitational waves can provide a unique view beyond the detector horizon, and it would be a shame if we missed them.

A Supplementary derivations

A.1 Point masses on stationary orbits

We take the binary black holes to be two point masses of m_1 and m_2 on a circular orbit of diameter R. Their positions $\mathbf{x})_{1,2}$ at time t are then given by

$$\begin{aligned}\mathbf{x}_1(t) &= R\frac{m_2}{m_1+m_2}\hat{e}(t) \quad = R\frac{\mu}{m_1}\hat{e}(t)\\ \mathbf{x}_2(t) &= -R\frac{m_1}{m_1+m_2}\hat{e}(t) = -R\frac{\mu}{m_2}\hat{e}(t)\,,\end{aligned}$$

with $\mu = m_1m_2/(m_1+m_2)$ the reduced mass and $\hat{e}(t)$ the unit vector pointing from the centre of mass to m_1

$$\hat{e}(t) = (\cos(\omega t), \cos(\iota)\sin(\omega t), \sin(\iota)\sin(\omega t))\,,$$

where ι is the inclination as is illustrated in Fig. 4, and ω is the orbital frequency. The mass quadrupole moment (Eq. (2.13)) can be approximated in the limit of non-relativistic velocities as

$$\begin{aligned}M^{ij}(t) &= \frac{1}{c^2}\int \mathrm{d}^3\mathbf{x}\, T^{00}(t,\mathbf{x})x^ix^j\\ &= \int \mathrm{d}^3\mathbf{x}\,\rho(t,\mathbf{x})x^ix^j\,,\end{aligned}$$

with $\rho(t,\mathbf{x})$ the density of the two point masses

$$\begin{aligned}\rho(t,\mathbf{x}) &= m_1\delta^3(\mathbf{x}-\mathbf{x}_1) + m_2\delta^3(\mathbf{x}-\mathbf{x_2})\\ &= m_1\delta^3\left(\mathbf{x}-\frac{\mu}{m_1}R\hat{e}(t)\right) + m_2\delta^3\left(\mathbf{x}+\frac{\mu}{m_2}R\hat{e}(t)\right)\,,\end{aligned}$$

where $\delta^3(\mathbf{x})$ is the three-dimensional Dirac-delta function. We can now solve the integral to get the mass quadrupole moments

$$\begin{aligned}M^{ij}(t) &= \int \mathrm{d}^3\mathbf{x}\left[m_1\delta^3\left(\mathbf{x}-\frac{\mu}{m_1}R\hat{e}(t)\right) + m_2\delta^3\left(\mathbf{x}+\frac{\mu}{m_2}R\hat{e}(t)\right)\right]x^ix^j\\ &= \int \mathrm{d}^3\mathbf{x}\, m_1x^ix^j\delta^3\left(\mathbf{x}-\frac{\mu}{m_1}R\hat{e}(t)\right) + \int \mathrm{d}^3\mathbf{x}\, m_2x^ix^j\delta^3\left(\mathbf{x}+\frac{\mu}{m_2}R\hat{e}(t)\right)\\ &= m_1\frac{\mu^2}{m_1^2}R^2\hat{e}_1\hat{e}_2 + m_2\frac{\mu^2}{m_2^2}R^2\hat{e}_1\hat{e}_2\\ &= \mu R^2\hat{e}_1\hat{e}_2\,,\end{aligned}$$

with $\hat{e}_{1,2}$ the first and second component of $\hat{e}$, respectively. Writing these out explicitly and differentiating twice with respect to time, we get

$$\begin{aligned}M^{11}(t) &= \mu R^2\cos^2(\omega t) &\rightarrow\quad \ddot{M}^{11}(t) &= -2\mu R^2\omega^2\cos(2\omega t)\\ M^{22}(t) &= \mu R^2\cos^2(\iota)\sin^2(\omega t) &\rightarrow\quad \ddot{M}^{22}(t) &= 2\mu R^2\omega^2\cos(2\omega t)\\ M^{12}(t) &= \mu R^2\cos(\iota)\cos(\omega t)\sin(\omega t) &\rightarrow\quad \ddot{M}^{12}(t) &= -2\mu R^2\omega^2\sin(2\omega t)\,.\end{aligned}$$

We can now substitute these into the definitions of the plus and cross polarisations (Eq. (2.14))

$$\begin{aligned}h_+ &= \frac{1}{r}\frac{G}{c^4}(\ddot{M}^{11}(t_{\mathrm{ret}}) - \ddot{M}^{22}(t_{\mathrm{ret}})) = -\frac{4}{r}\frac{G}{c^4}\mu R^2\frac{1+\cos(\iota)}{2}\cos(2\omega t_{\mathrm{ret}})\\ h_\times &= \frac{2}{r}\frac{G}{c^4}\ddot{M}^{12}(t_{\mathrm{ret}}) \qquad\qquad = -\frac{4}{r}\frac{G}{c^4}\mu R^2\cos(\iota)\sin(2\omega t_{\mathrm{ret}})\,.\end{aligned}$$

However, the quantities R, μ and ω are not independent from each other, but related through Kepler's third law:

$$\frac{R^3}{\omega^2} = GM\,,$$

where $M = m_1 + m_2$ the total mass of the system. Introducing the chirp mass

$$\mathcal{M}_c = \frac{(m_1 m_2)^{3/5}}{(m_1 + m_2)^{1/5}} = \mu^{3/5} M^{2/5} \,,$$

we finally arrive at our desired result, Eq. (2.15)

$$h_+ = -\frac{4}{r}\left(\frac{G\mathcal{M}_c}{c^2}\right)^{5/3}\left(\frac{\omega}{c}\right)^{2/3}\frac{1+\cos^2(\iota)}{2}\cos(2\omega t_{\rm ret})$$
$$h_\times = -\frac{4}{r}\left(\frac{G\mathcal{M}_c}{c^2}\right)^{5/3}\left(\frac{\omega}{c}\right)^{2/3}\cos(\iota)\sin(2\omega t_{\rm ret})\,.$$

A.2 The optical depth

The total probability of a source at redshift z_s being strongly lensed can be expressed as an integral over the conditional probabilities

$$p(\mathrm{SL}|\mathrm{z_s}) = \int \mathrm{p}(\mathrm{SL}|\mathrm{z_s}, \mathrm{z_L}, \boldsymbol{\theta}_\mathrm{L})\mathrm{p}(\mathrm{z_L}, \boldsymbol{\theta}_\mathrm{L}|\mathrm{z_s})\mathrm{dz_L}\mathrm{d}\boldsymbol{\theta}_\mathrm{L}\,,$$

where $p(\mathrm{SL}|\mathrm{z_s}, \mathrm{z_L}, \boldsymbol{\theta}_\mathrm{L})$ is the probability of a single galaxy-lens with parameters $\boldsymbol{\theta}_L$ at redshift z_L lensing a source at z_s

$$p(\mathrm{SL}|\mathrm{z_s}, \mathrm{z_L}, \boldsymbol{\theta}_\mathrm{L}) = \frac{\pi\theta_\mathrm{E}^2}{4\pi}\,,$$

and $p(z_L, \boldsymbol{\theta}_L|z_s)$ is the probability of finding such a lens

$$p(z_L, \boldsymbol{\theta}_L|z_s) = \frac{\mathrm{d}^2 N_\ell}{\mathrm{d}z_L \mathrm{d}\boldsymbol{\theta}_L} = \frac{\mathrm{d}^2 N_\ell}{\mathrm{d}V_c \mathrm{d}\boldsymbol{\theta}_L}\frac{\mathrm{d}V_c}{\mathrm{d}z_L} = \frac{\mathrm{d}n_\ell}{\mathrm{d}\boldsymbol{\theta}_L}\frac{\mathrm{d}V_c}{\mathrm{d}z_L} = n_\ell^0\, p(\boldsymbol{\theta}_L)\frac{\mathrm{d}V_c}{\mathrm{d}z_L}\,.$$

Here, $N_\ell(z_L, \boldsymbol{\theta}_L)$ is the total number of lenses and n_ℓ is the number-density of lenses. We take n_ℓ^0 to be independent of $\boldsymbol{\theta}_L$, such that $\mathrm{d}n_\ell/\mathrm{d}\boldsymbol{\theta}_L$ follows the distribution of lens parameters $p(\boldsymbol{\theta}_L)$, normalised by the constant number density n_ℓ^0. We approximate the lenses as spherically symmetric (SIS model), which leaves the velocity dispersion σ_v as the only lens parameter.

We now take $\tau(z_s)$ the optical depth to be $p(\mathrm{SL}|\mathrm{z_s})$, and substitute the different probabilities:

$$\tau(z_s) = \int_0^{z_s}\mathrm{d}z_L \int_0^\infty \mathrm{d}\sigma_v\, n_\ell^0 \frac{\theta_E^2}{4}\frac{\mathrm{d}V_c}{\mathrm{d}z_L}p(\sigma_v)\,,$$

where $p(\sigma_v)$ is given by

$$p(\sigma_v) = \frac{1}{\sigma^*}\left(\frac{\sigma_v}{\sigma^*}\right)^{\alpha-1} e^{-\left(\frac{\sigma_v}{\sigma^*}\right)^\beta}\frac{\beta}{\Gamma(\alpha/\beta)}\,,$$

with $\alpha = 2.32$, $\beta = 2.67$, $\sigma^* = 161$ km s^{-1} and Γ the Gamma function defined for $\mathrm{Re}(z) > 0$

$$\Gamma(z) = \int_0^\infty \mathrm{d}x\, x^{z-1}e^{-x}\,.$$

Together with the expression for the Einstein radius (Eq. (3.15)), which carries a σ_v^2 term, we can now carry out the integration:

$$\begin{aligned}
\tau(z_s) &= 4\pi^2 n_\ell^0\left(\frac{\sigma^*}{c}\right)^4\int_0^{z_s}\mathrm{d}z_L\frac{\mathrm{d}V_c}{\mathrm{d}z_L}\left(\frac{D_{LS}}{D_S}\right)^2\int_0^\infty \mathrm{d}\left(\frac{\sigma_v}{\sigma^*}\right)\left(\frac{\sigma_v}{\sigma^*}\right)^{3+\alpha}e^{-\left(\frac{\sigma_v}{\sigma^*}\right)^\beta}\frac{\beta}{\Gamma(\alpha/\beta)} \\
&= 4\pi^2 n_\ell^0\left(\frac{\sigma^*}{c}\right)^4\int_0^{z_s}\mathrm{d}z_L\frac{\mathrm{d}V_c}{\mathrm{d}z_L}\left(\frac{D_{LS}}{D_S}\right)^2\int_0^\infty \mathrm{d}x\, x^{\frac{4+\alpha-\beta}{\beta}}e^{-x}\frac{1}{\Gamma(\alpha/\beta)}\,,\ \text{where } x = \left(\frac{\sigma_v}{\sigma^*}\right)^\beta \\
&= 4\pi^2 n_\ell^0\left(\frac{\sigma^*}{c}\right)^4\frac{\Gamma([4+\alpha]/\beta)}{\Gamma(\alpha/\beta)}\int_0^{z_s}\mathrm{d}z_L\frac{\mathrm{d}V_c}{\mathrm{d}z_L}\left(\frac{D_{LS}}{D_S}\right)^2\,,
\end{aligned}$$

use $V_c = \frac{4}{3}\pi r^3$ and $D_{LS} = \frac{r(z_s)-r(z_L)}{1+z_s}$:

$$
\begin{aligned}
&= 4\pi^2 n_\ell^0 \left(\frac{\sigma^*}{c}\right)^4 \frac{\Gamma([4+\alpha]/\beta)}{\Gamma(\alpha/\beta)} \int_0^{z_s} \mathrm{d}z_L \, 4\pi r^2(z_L) \frac{\mathrm{d}r}{\mathrm{d}z_L} \left(1 - \frac{r(z_L)}{r(z_s)}\right)^2 \\
&= 16\pi^3 n_\ell^0 \left(\frac{\sigma^*}{c}\right)^4 \frac{\Gamma([4+\alpha]/\beta)}{\Gamma(\alpha/\beta)} r^3(z_s) \int_0^1 \mathrm{d}y \, y^2(1-y)^2 \,, \text{ where } y = \frac{r(z_L)}{r(z_s)} \\
&= 16\pi^3 n_\ell^0 \left(\frac{\sigma^*}{c}\right)^4 \frac{\Gamma([4+\alpha]/\beta)}{\Gamma(\alpha/\beta)} \frac{r^3(z_s)}{30} \,.
\end{aligned}
$$

The number density for early-type galaxies from the SDSS catalogue was found by [65], and is given by $n_\ell^0 = 8 \times 10^{-3} h^3$ Mpc^{-3}, with $h = H_0/(100$ km s^{-1} Mpc$^{-1})$ the dimensionless Hubble constant. Plugging in all the values for the constants, we get our final result, Eq. (4.12):

$$
\tau(z_s) \approx 4.17 \times 10^{-6} \left(\frac{r(z_s)}{1 \text{ Gpc}}\right)^3 \,.
$$

B A Comprehensive Guide to Everything Gravity[6]

According to Igitur Statistics, only a small percentage of people actually read my entire thesis. So if you end up enjoying this summary, please consider reading the thesis from start to finish. It is completely free, and you can always change your mind later.

In Einstein's general relativity, space and time are no longer separate quantities, but are instead connected through the medium of *spacetime*. Spacetime is not necessarily Euclidean (like all the neat little perpendicular lines on graph paper), it can be curved instead. This curvature is caused by the presence of mass (or equivalently, energy), and can be visualised as follows. Imagine a trampoline that you place a bowling ball on top of. The trampoline sheet will curve down, just like spacetime curves around a single massive object. Suppose you now take a ping-pong ball, place it at a certain distance away from the bowling ball, and give it a push. If given the right push[7], the ping-pong ball will start circling the bowling ball, much like the Earth orbiting the Sun.

Suppose that instead of a ping-pong ball, we would take out a second bowling ball, and push both bowling balls in opposite directions. They would start orbiting each other, not unlike two black holes. *Black holes* are curious astrophysical objects with all their mass concentrated in a single point, the singularity. They curve spacetime so strongly that beyond a radius called the event horizon, nothing can escape, not even light. In our trampoline analogy, they are the ultimate bowling balls, though you cannot throw them as they are infinitely small. Two black holes together form a binary black hole system.

The orbiting black holes continuously alter the local curvature of spacetime as their positions change over time. These periodical changes of the curvature manifest themselves as *gravitational waves*, which can be visualised as the trampoline surface becoming extremely bouncy. The gravitational waves carry away energy, as changing the curvature of spacetime comes at a cost. Since total energy needs to be conserved, the black holes start slowly spiralling inwards, as their orbital energy decreases. This continues until the innermost stable circular orbit is reached, and the black holes plummet towards each other, before finally merging and forming a single, larger black hole. This entire process is called *coalescence*.

As the gravitational waves travel through spacetime, there is a chance of them encountering a galaxy or galaxy cluster. These massive astrophysical objects are approximately stationary while the waves pass by,

[6] Terms and services apply. The author does not claim this section to be an accurate representation of the theory of General Relativity.

[7] On a frictionless trampoline, the existence of which might be debatable.

so their effect on spacetime is only dependent on the space part. Kind of like our single bowling ball at the beginning, but extremely large, massive and possibly asymmetric in shape. The path of the gravitational wave gets deflected as it has to follow the curved space. This is called *gravitational lensing*, and is quite commonly observed for light[8].

After being lensed by a galaxy or galaxy cluster, the gravitational wave moves on into the vast emptiness that is most of our Universe. However, there is a tiny chance of it encountering a certain small blue planet, orbiting an unremarkable yellow sun in the unfashionable end of the Western Spiral Arm of the Milky Way [78]. There, it will pass through some funky machine made by little men, consisting of two perpendicular arms, each 4 km long. These arms will be alternately stretched and squished by about a thousandth the size of a proton, as the gravitational wave passes. Through many an engineering and data analysis feat, we can measure these changes in length, and thus detect these gravitational waves.

At the source, the gravitational waves fly out in all directions, with each direction having an uniquely determined path. Through strong gravitational lensing, different paths can combine at a single point. We observe this as multiple images of the same object, but appearing at different positions in the sky (see Fig. 6 for a nice photo from the Hubble telescope). Gravitational-wave detectors (the funky machines) do not have the resolution to see the differences between the sky positions, but they can measure other effects. The amplitude of the waves is magnified differently for each image, and they arrive at separate times due to the difference in the path length. We can thus measure a lensed gravitational wave as repeated events in our detector, with different amplitudes but with the same general form.

The goal of my thesis is to make predictions about these observed lensed gravitational waves. How many can we expect to see, in coming years and farther away in the future? What are the properties of these detections, and can we use these predictions to our advantage? This reveals the true topic of this work: statistics. If we want to say anything meaningful, we need to build a large dataset containing the properties of the lensed gravitational waves. These properties follow distributions, which tell us the how often a certain value of a property occurs with respect to the total population. An example of a distribution can be found in Fig. 9, which shows the distribution for the mass of the heaviest black hole of the binary. It has two peaks and an overly complicated formula that comes with it, but we will ignore that struggle here.

This specific distribution for the mass has been inferred from the currently available data by the LIGO-Virgo Collaboration. LIGO has two detectors in the United States, LIGO-Livingston and LIGO-Hanford, while Virgo is a single detector in Italy. Together, they have about 50 publicly released detections of gravitational waves, and are currently working on the data analysis for even more. The mass distribution of these 50 detections is not the distribution we will use. Heavy black holes generate gravitational waves with larger amplitudes, and are thus easier to detect. This effect is called the observational bias. We can make educated guesses about this bias, and correct our observed distributions for it. This gives us an idea of what the true population looks like. We will be using these distributions of the true populations in this thesis. Note however, that these are not set in stone. They are guesses, as that is the best thing we have.

Masses are not the only thing we need for our population of lensed gravitational waves. We place the binaries a certain distance[9] away, and throw a bunch of orientation angles into the fray (see Fig. 4 for an illustration of all the different angles). This gives us all the necessary details of the unlensed gravitational wave. We then turn our attention to the galaxies that will lens them. From observations with optical telescopes and other astronomical machinery, distributions for the sizes, shapes and mass-density profiles of galaxy-lenses have been inferred. These are all the distributions we care about in this thesis.

We calculate the effects of lensing on the gravitational waves with the LENSTRONOMY package, and quantify the signal 'loudness' with PYCBC. Remember the lengthy explanation of black holes, gravitational waves and gravitational lensing I gave earlier? I do not do any of the associated calculations myself, I just use the code

[8] A single Google search on "gravitational lensing hubble telescope" will show you a plethora of pretty pictures.

[9] Sec. 2.1 explains how our regular notion of distance is broken in an expanding Universe, but I will not bother you about that here.

other people have been developing for years or even decades. I did, however, write a bunch of routines for drawing samples from all of the distributions I need. Binary black hole properties get thrown at PYCBC, while galaxy properties are chugged at LENSTRONOMY. Combining the results from the two, I get all the data I need for a single lensed gravitational wave: values for the properties of the binary black holes, the galaxy-lens and the observed gravitational wave.

You cannot do statistics with a single event (the lensed gravitational wave), so we need a couple more. A million in our case, to be precise, so that the random samples accurately form the entire distribution they were sampled from. This takes quite a long time to do, and I would like to be able to use my laptop for other things. Luckily, I had access to LIGO's CIT computational cluster at Caltech. Through some old-fashioned command-line work[10], I had my codes run on a random computing core in California, waited half a day for them to finish, and then copied the results back to my own laptop. Since we have quite large number of black holes, and a dozen properties to be recorded, my results were in the form 400 MB of doom contained in a single .txt file.

We can now finally move on to the actual results. We start with calculating the predicted number of observed lensed events per year. There are some big tables in the results section, quoting all sorts of numbers. However, our main prediction is $1-2$ lensed events per year with four operational detectors at their target sensitivity (sensitivity quantifies the noise levels in a detector). We thus conclude that lensed event observations become quite probable in the near future, justifying why research should be done to prepare for them. The actual number of observations will provide valuable information as well. The predictions we make are highly dependent on a number of choices, assumptions and inferred populations. Different models predict different observed event rates, so (non-)detection can tell us more about which of our assumptions are consistent with the true population.

Our second question is more involved: what are the properties of the expected detections and can we use this information to our advantage? Extracting the properties is easy, those are in the .txt file. Sec. 5.2 shows the distributions for the time delays between different images of the same lensed system, and some further categorisation of these systems. Sec. 5.4 shows two examples of distributions for properties of the source binary black holes and of the galaxy lenses. Sec. 5.3 discusses the effect of the time-delay distributions on the lensed event searches, so I will explain those searches first.

A search is an analysis of detector data in order to find gravitational wave signals. Strongly lensed gravitational waves appear as multiple images with different amplitudes at different arrival times, but with a similar detector signature. Strong lensing searches thus compare the match in detector signatures between all gravitational-wave detections. However, it is entirely possible for two gravitational waves to have a similar signature through pure coincidence. We call this a *false alarm*, and pairs of gravitational waves have an intrinsic false alarm probability. The number of pairs grows quadratically with the number of detections, making the occurrence of a false alarm essentially inevitable. This is disastrous, as any lensed event candidates could now be challenged based on this inevitability.

We suggest the inclusion of the time-delay distributions to combat this catastrophe, and show a proof of concept. Randomly chosen pairs of unlensed events can have any time delay between them, but we showed in Sec. 5.2 that lensed events have quite typical time-delays. We then do some statistical jujitsu to quantify when a pair of unlensed events produces a similar time-delay to lensed events. If a time-delay is unlikely to come from a lensed event, we reduce the individual false alarm probability of the unlensed pair. Repeat this for a significant amount of unlensed event pairs, and you get Fig. 16b, which shows a significant reduction in the total false alarm probability. We thus argue that the inclusion of time-delay distributions is vital for the lensed event searches.

And that's all folks! We find that a lensed event detection becomes increasingly probable in the future, and we underline the importance of statistical predictions for the searches. The 400 MB of doom are available online [71] for anyone to have a go at. For now, I will deactivate. Renske out.

[10] Graphical interfaces are for casuals and I do not take constructive criticism.

Acknowledgements

I could not have come this far without the help of many others. I want to thank Otto Hannuksela for the supervising, answering all of my mails and pushing me to further heights. I have greatly enjoyed working together. I would also like to thank Chris van den Broeck for the supervising and the positivity, you have given me so many confidence boosts. My gratitude goes out to Ewoud Wempe and Leon Koopmans as well, you have both been extremely helpful in providing feedback during the paper writing process. Ewoud was also a true mvp for finding many a bug/typo in the code. I want to thank Justin Janquart, Tjonnie Li, Chun Lung Chan and Alvin Li for the fruitful discussions we had. Shout out to my close friend and flatmate Cintia Perugachi for listening to me talk about code and distributions for almost an entire year. Cheers to Leon Kamermans for joining me on this journey of gravitational-wave research and being an amazing friend. Last but not least, I want to thank Philza for the consistent entertainment the past year.[11]

A.R.A.C.W., O.A.H, and C.V.D.B. are supported by the research program of the Netherlands Organisation for Scientific Research (NWO). The authors are grateful for computational resources provided by the LIGO Laboratory and supported by the National Science Foundation Grants No. PHY-0757058 and No. PHY-0823459.

[11] And thanks to my younger brother I guess, who requested to be mentioned here.

References

[1] Albert Einstein. "Die Grundlage der allgemeinen Relativitätstheorie". In: *Annalen der Physik* 354.7 (1916), pp. 769–822. DOI: 10.1002/andp.19163540702.

[2] Frank Watson Dyson, Arthur Stanley Eddington, and C. Davidson. "IX. A determination of the deflection of light by the sun's gravitational field, from observations made at the total eclipse of May 29, 1919". In: *Philosophical Transactions of the Royal Society of London. Series A., Containing Papers of a Mathematical or Physical Character* 220 (1920), pp. 291–333. DOI: 10.1098/rsta.1920.0009.

[3] D. Walsh, R. F. Carswell, and R. J. Weymann. "0957 + 561 A, B: twin quasistellar objects or gravitational lens?" In: *Nature* 279 (1979), pp. 381–384. DOI: 10.1038/279381a0.

[4] R. Laureijs et al. *Euclid Definition Study Report*. 2011. arXiv: 1110.3193 [astro-ph.CO].

[5] M. T. Penny et al. "ExELS: an exoplanet legacy science proposal for the ESA Euclid mission – I. Cold exoplanets". In: *Monthly Notices of the Royal Astronomical Society* 434.1 (July 2013), pp. 2–22. ISSN: 1365-2966. DOI: 10.1093/mnras/stt927.

[6] I. McDonald et al. "ExELS: an exoplanet legacy science proposal for the ESA Euclid mission - II. Hot exoplanets and sub-stellar systems". In: *Monthly Notices of the Royal Astronomical Society* 445.4 (Nov. 2014), pp. 4137–4154. ISSN: 1365-2966. DOI: 10.1093/mnras/stu2036.

[7] Karl Schwarzschild. "Über das Gravitationsfeld eines Massenpunktes nach der Einsteinschen Theorie". In: *Sitzungsberichte der Königlich Preußischen Akademie der Wissenschaften (Berlin* (Jan. 1916), pp. 189–196.

[8] "Physical Sciences: Detection of Radio Emission from Cygnus X-1". In: *Nature* 232.246 (1971). DOI: 10.1038/232246a0.

[9] J. Kristian et al. "On the Optical Identification of Cygnus X-1". In: *Astrophysical J.* 168 (Sept. 1971), p. L91. DOI: 10.1086/180790.

[10] The Event Horizon Telescope Collaboration et al. "First M86 Event Horizon Telescope Results I. The Shadow of the Supermassive Black Hole". In: *The Astrophysical Journal Letters* 875.1 (2019). DOI: 10.3847/2041-8213/ab0ec7.

[11] Albert Einstein. "Näherungsweise Integration der Feldgleichungen der Gravitation". In: *Sitzungsberichte der Königlich Preußischen Akademie der Wissenschaften (Berlin* (Jan. 1916), pp. 688–696. DOI: 10.1002/3527608958.ch7.

[12] J. M. Weisberg, J. H. Taylor, and L. A. Fowler. "Gravitational waves from an orbiting pulsar". In: *Scientific American* 245 (Oct. 1981), pp. 74–82. DOI: 10.1038/scientificamerican1081-74.

[13] J. M. Weisberg and Y. Huang. "Relativistic Measurements from Timing the Binary Pulsar PSR B1913+16". In: *The Astrophysical Journal* 829.1 (Sept. 2016), p. 55. ISSN: 1538-4357. DOI: 10.3847/0004-637x/829/1/55.

[14] B. P. Abbott et al. "Observation of Gravitational Waves from a Binary Black Hole Merger". In: *Phys. Rev. Lett.* 116 (6 Feb. 2016), p. 061102. DOI: 10.1103/PhysRevLett.116.061102.

[15] R. Abbott et al. *GWTC-2: Compact Binary Coalescences Observed by LIGO and Virgo During the First Half of the Third Observing Run*. 2021. arXiv: 2010.14527 [gr-qc].

[16] H.C. Ohanian. "On the focusing of gravitational radiation". In: *Int. J. Theor. Phys.* 9 (1974), pp. 425–437. DOI: 10.1007/BF01810927.

[17] K.S. Thorne. "The Theory of Gravitational Radiation: An Introductory Review". In: *Les Houches Summer School on Gravitational Radiation*. Jan. 1982, pp. 1–57.

[18] Shuji Deguchi and William D. Watson. "Wave effects in gravitational lensing of electromagnetic radiation". In: *Phys. Rev. D* 34 (1986), pp. 1708–1718. DOI: 10.1103/PhysRevD.34.1708.

[19] Yun Wang, Albert Stebbins, and Edwin L. Turner. "Gravitational lensing of gravitational waves from merging neutron star binaries". In: *Phys. Rev. Lett.* 77 (1996), pp. 2875–2878. DOI: 10.1103/PhysRevLett.77.2875. arXiv: astro-ph/9605140.

[20] Takahiro T. Nakamura. "Gravitational lensing of gravitational waves from inspiraling binaries by a point mass lens". In: *Phys. Rev. Lett.* 80 (1998), pp. 1138–1141. DOI: 10.1103/PhysRevLett.80.1138.

[21] Ryuichi Takahashi and Takashi Nakamura. "Wave effects in gravitational lensing of gravitational waves from chirping binaries". In: *Astrophys. J.* 595 (2003), pp. 1039–1051. DOI: 10.1086/377430. arXiv: astro-ph/0305055.

[22] Liang Dai and Tejaswi Venumadhav. "On the waveforms of gravitationally lensed gravitational waves". In: (Feb. 2017). arXiv: 1702.04724 [gr-qc].

[23] Otto A. Hannuksela et al. "Localizing merging black holes with sub-arcsecond precision using gravitational-wave lensing". In: (Apr. 2020). DOI: 10.1093/mnras/staa2577. arXiv: 2004.13811 [astro-ph.HE].

[24] M. Sereno et al. "Cosmography with strong lensing of LISA gravitational wave sources". In: *Mon. Not. Roy. Astron. Soc.* 415 (2011), p. 2773. DOI: 10.1111/j.1365-2966.2011.18895.x. arXiv: 1104.1977 [astro-ph.CO].

[25] Kai Liao et al. "Precision cosmology from future lensed gravitational wave and electromagnetic signals". In: *Nature Commun.* 8.1 (2017). [Erratum: Nature Commun. 8, 2136 (2017)], p. 1148. DOI: 10.1038/s41467-017-01152-9. arXiv: 1703.04151 [astro-ph.CO].

[26] Shuo Cao et al. "Direct test of the FLRW metric from strongly lensed gravitational wave observations". In: *Sci. Rep.* 9.1 (2019), p. 11608. DOI: 10.1038/s41598-019-47616-4. arXiv: 1910.10365 [astro-ph.CO].

[27] Yufeng Li, Xilong Fan, and Lijun Gou. "Constraining Cosmological Parameters in the FLRW Metric with Lensed GW+EM Signals". In: *Astrophys. J.* 873.1 (2019), p. 37. DOI: 10.3847/1538-4357/ab037e. arXiv: 1901.10638 [astro-ph.CO].

[28] Tessa Baker and Mark Trodden. "Multimessenger time delays from lensed gravitational waves". In: *Phys. Rev. D* 95.6 (2017), p. 063512. DOI: 10.1103/PhysRevD.95.063512. arXiv: 1612.02004 [astro-ph.CO].

[29] Xi-Long Fan et al. "Speed of Gravitational Waves from Strongly Lensed Gravitational Waves and Electromagnetic Signals". In: *Phys. Rev. Lett.* 118.9 (2017), p. 091102. DOI: 10.1103/PhysRevLett.118.091102. arXiv: 1612.04095 [gr-qc].

[30] Suvodip Mukherjee, Benjamin D. Wandelt, and Joseph Silk. "Multimessenger tests of gravity with weakly lensed gravitational waves". In: *Phys. Rev. D* 101.10 (2020), p. 103509. DOI: 10.1103/PhysRevD.101.103509. arXiv: 1908.08950 [astro-ph.CO].

[31] Suvodip Mukherjee, Benjamin D. Wandelt, and Joseph Silk. "Probing the theory of gravity with gravitational lensing of gravitational waves and galaxy surveys". In: *Mon. Not. Roy. Astron. Soc.* 494.2 (2020), pp. 1956–1970. DOI: 10.1093/mnras/staa827. arXiv: 1908.08951 [astro-ph.CO].

[32] Srashti Goyal et al. "Testing the nature of gravitational-wave polarizations using strongly lensed signals". In: *Physical Review D* 103.2 (Jan. 2021). ISSN: 2470-0029. DOI: 10.1103/physrevd.103.024038.

[33] Ken K.Y. Ng et al. "Precise LIGO Lensing Rate Predictions for Binary Black Holes". In: *Phys. Rev. D* 97.2 (2018), p. 023012. DOI: 10.1103/PhysRevD.97.023012. arXiv: 1703.06319 [astro-ph.CO].

[34] Shun-Sheng Li et al. "Gravitational lensing of gravitational waves: A statistical perspective". In: *Mon. Not. Roy. Astron. Soc.* 476.2 (2018), pp. 2220–2229. DOI: 10.1093/mnras/sty411. arXiv: 1802.05089 [astro-ph.CO].

[35] Masamune Oguri. "Effect of gravitational lensing on the distribution of gravitational waves from distant binary black hole mergers". In: *Mon. Not. Roy. Astron. Soc.* 480.3 (2018), pp. 3842–3855. DOI: 10.1093/mnras/sty2145. arXiv: 1807.02584 [astro-ph.CO].

[36] Fei Xu, Jose Maria Ezquiaga, and Daniel E. Holz. "Please repeat: Strong lensing of gravitational waves as a probe of compact binary and galaxy populations". In: (May 2021). arXiv: 2105.14390 [astro-ph.CO].

[37] Suvodip Mukherjee et al. "Impact of astrophysical binary coalescence timescales on the rate of lensed gravitational wave events". In: (June 2021). arXiv: 2106.00392 [gr-qc].

[38] Zhoujian Cao, Li-Fang Li, and Yan Wang. "Gravitational lensing effects on parameter estimation in gravitational wave detection with advanced detectors". In: *Phys. Rev. D* 90.6 (2014), p. 062003. DOI: 10.1103/PhysRevD.90.062003.

[39] Kwun-Hang Lai et al. "Discovering intermediate-mass black hole lenses through gravitational wave lensing". In: *Phys. Rev. D* 98.8 (2018), p. 083005. DOI: 10.1103/PhysRevD.98.083005. arXiv: 1801.07840 [gr-qc].

[40] K. Haris et al. "Identifying strongly lensed gravitational wave signals from binary black hole mergers". In: (July 2018). arXiv: 1807.07062 [gr-qc].

[41] Peter T.H. Pang et al. "Lensed or not lensed: Determining lensing magnifications for binary neutron star mergers from a single detection". In: (Feb. 2020). DOI: 10.1093/mnras/staa1430. arXiv: 2002.04893 [astro-ph.HE].

[42] Giulia Pagano, Otto A. Hannuksela, and Tjonnie G.F. Li. "lensingGW: a Python package for lensing of gravitational waves". In: (June 2020). arXiv: 2006.12879 [astro-ph.CO].

[43] Rico K. L. Lo and Ignacio Magaña Hernandez. "A Bayesian statistical framework for identifying strongly-lensed gravitational-wave signals". In: (Apr. 2021). arXiv: 2104.09339 [gr-qc].

[44] Justin Janquart et al. *A fast and precise methodology to search for and analyse strongly lensed gravitational-wave events*. May 2021. arXiv: 2105.04536 [gr-qc].

[45] O.A. Hannuksela et al. "Search for gravitational lensing signatures in LIGO-Virgo binary black hole events". In: *Astrophys. J. Lett.* 874.1 (2019), p. L2. DOI: 10.3847/2041-8213/ab0c0f. arXiv: 1901.02674 [gr-qc].

[46] Xiaoshu Liu, Ignacio Magana Hernandez, and Jolien Creighton. "Identifying strong gravitational-wave lensing during the second observing run of Advanced LIGO and Advanced Virgo". In: (Sept. 2020). arXiv: 2009.06539 [astro-ph.HE].

[47] Liang Dai et al. "Search for Lensed Gravitational Waves Including Morse Phase Information: An Intriguing Candidate in O2". In: (July 2020). arXiv: 2007.12709 [astro-ph.HE].

[48] R. Abbott et al. "Search for lensing signatures in the gravitational-wave observations from the first half of LIGO-Virgo's third observing run". In: (May 2021). arXiv: 2105.06384 [gr-qc].

[49] A. Renske A. C. Wierda et al. *Beyond the detector horizon: Forecasting gravitational-wave strong lensing*. June 2021. arXiv: 2106.06303 [astro-ph.HE].

[50] Barbara Ryden. *Introduction to Cosmology*. 2nd ed. Cambridge University Press, 2016. DOI: 10.1017/9781316651087.

[51] Jolien D. E. Creighton and Warren G. Anderson. *Gravitational-Wave Physics and Astronomy: An Introduction to Theory, Experiment and Data Analysis*. 1st ed. John Wiley & Sons, Incorporated, 2011. ISBN: 9783527408863.

[52] Luc Blanchet. "Gravitational Radiation from Post-Newtonian Sources and Inspiraling Compact Binaries". In: *Living Reviews in Relativity* 17.1 (Feb. 2014). ISSN: 1433-8351. DOI: 10.12942/lrr-2014-2.

[53] Michele Maggiore. *Gravitational Waves: Volume 1: Theory and Experiments*. Oxford University Press, 2008. DOI: 10.1093/acprof:oso/9780198570745.001.0001.

[54] S. A. Kaplan. "On circular orbits in Einstein's Gravitation Theory". In: *Zhurnal Eksperimentalnoi i Teoreticheskoi Fiziki* 19 (Jan. 1949), pp. 951–952.

[55] Sascha Husa et al. "Frequency-domain gravitational waves from nonprecessing black-hole binaries. I. New numerical waveforms and anatomy of the signal". In: *Physical Review D* 93.4 (Feb. 2016). ISSN: 2470-0029. DOI: 10.1103/physrevd.93.044006.

[56] B. S. Sathyaprakash and Bernard F. Schutz. "Physics, Astrophysics and Cosmology with Gravitational Waves". In: *Living Reviews in Relativity* 12.1 (Mar. 2009). ISSN: 1433-8351. DOI: 10.12942/lrr-2009-2.

[57] B. P. Abbott et al. "Prospects for observing and localizing gravitational-wave transients with Advanced LIGO, Advanced Virgo and KAGRA". In: *Living Rev. Rel.* 23.1 (2020), p. 3. DOI: 10.1007/s41114-020-00026-9.

[58] Ramesh Narayan and Matthias Bartelmann. *Lectures on Gravitational Lensing*. 1996. arXiv: astro-ph/9606001.

[59] S. H. Suyu et al. "Two accurate time-delay distances from strong lensing: Implications for cosmology". In: *The Astrophysical Journal* 766.2 (Mar. 2013), p. 70. ISSN: 1538-4357. DOI: 10.1088/0004-637x/766/2/70.

[60] Andrew Robertson et al. "What does strong gravitational lensing? The mass and redshift distribution of high-magnification lenses". In: (Feb. 2020). DOI: 10.1093/mnras/staa1429. arXiv: 2002.01479 [astro-ph.CO].

[61] R. Abbott et al. "Population Properties of Compact Objects from the Second LIGO-Virgo Gravitational-Wave Transient Catalog". In: (Oct. 2020). arXiv: 2010.14533 [astro-ph.HE].

[62] Leon V. E. Koopmans et al. "The Sloan Lens ACS Survey. III. The Structure and Formation of Early-Type Galaxies and Their Evolution since z 1". In: *The Astrophysical Journal* 649.2 (Oct. 2006), pp. 599–615. ISSN: 1538-4357. DOI: 10.1086/505696.

[63] Thomas E Collett. "The population of galaxy-galaxy strong lenses in forthcoming optical imaging surveys". In: *Astrophys. J.* 811.1 (2015), p. 20. DOI: 10.1088/0004-637X/811/1/20. arXiv: 1507.02657 [astro-ph.CO].

[64] L. V. E. Koopmans et al. "The Structure and Dynamics of Massive Early-type Galaxies: On Homology, Isothermality, and Isotropy inside One Effective Radius". In: *The Astrophysical Journal* 703.1 (Sept. 2009), pp. L51–L54. ISSN: 1538-4357. DOI: 10.1088/0004-637x/703/1/l51.

[65] Yun-Young Choi, Changbom Park, and Michael S. Vogeley. "Internal and Collective Properties of Galaxies in the Sloan Digital Sky Survey". In: *Astrophys. J.* 658.2 (Apr. 2007), pp. 884–897. DOI: 10.1086/511060. arXiv: astro-ph/0611607 [astro-ph].

[66] Simon Birrer and Adam Amara. "Lenstronomy: multi-purpose gravitational lens modelling software package". In: (Mar. 2018). DOI: 10.1016/j.dark.2018.11.002. arXiv: 1803.09746 [astro-ph.CO].

[67] Simon Birrer et al. "lenstronomy II: A gravitational lensing software ecosystem". In: *Journal of Open Source Software* 6.62 (2021), p. 3283. DOI: 10.21105/joss.03283.

[68] Javier Roulet et al. "Binary black hole mergers from LIGO/Virgo O1 and O2: Population inference combining confident and marginal events". In: *Physical Review D* 102.12 (Dec. 2020). ISSN: 2470-0029. DOI: 10.1103/physrevd.102.123022.

[69] Sebastian Khan et al. "Frequency-domain gravitational waves from nonprecessing black-hole binaries. II. A phenomenological model for the advanced detector era". In: *Physical Review D* 93.4 (Feb. 2016). ISSN: 2470-0029. DOI: 10.1103/physrevd.93.044007.

[70] LIGO Scientific Collaboration. *LIGO Algorithm Library - LALSuite*. free software (GPL). 2018. DOI: 10.7935/GT1W-FZ16.

[71] A. Renske A. C. Wierda et al. *Catalogue of lensed gravitational wave events*. June 2021. DOI: 10.5281/zenodo.4905030.

[72] Alvin K.Y. Li et al. "Targeted Sub-threshold Search for Strongly-lensed Gravitational-wave Events". In: (Apr. 2019). arXiv: 1904.06020 [gr-qc].

[73] Connor McIsaac et al. "Search for Strongly Lensed Counterpart Images of Binary Black Hole Mergers in the First Two LIGO Observing Runs". In: (Dec. 2019). arXiv: 1912.05389 [gr-qc].

[74] Suvodip Mukherjee et al. "Inferring the lensing rate of LIGO-Virgo sources from the stochastic gravitational wave background". In: (June 2020). arXiv: 2006.03064 [astro-ph.CO].

[75] Graham P. Smith et al. "Strong-lensing of Gravitational Waves by Galaxy Clusters". In: *Proceedings of the International Astronomical Union* 13.S338 (Oct. 2017), pp. 98–102. ISSN: 1743-9221. DOI: 10.1017/s1743921318003757.

[76] M. Bernardi et al. "Galaxy Luminosities, Stellar Masses, Sizes, Velocity Dispersions as a Function of Morphological Type". In: 404 (June 2010), pp. 2087–2122. ISSN: 0035-8711. DOI: 10.1111/j.1365-2966.2010.16425.x.

[77] Katerina Chatziioannou, Nicolás Yunes, and Neil Cornish. "Model-independent test of general relativity: An extended post-Einsteinian framework with complete polarization content". In: *Phys. Rev. D* 86 (2 July 2012), p. 022004. DOI: 10.1103/PhysRevD.86.022004.

[78] Douglas Adams. *The Hitchhiker's Guide to the Galaxy*. Longmeadow Press, 1987. ISBN: 0-681-40322-5.